Univerzita Karlova v Praze
Matematicko-fyzikální fakulta

DIPLOMOVÁ PRÁCE

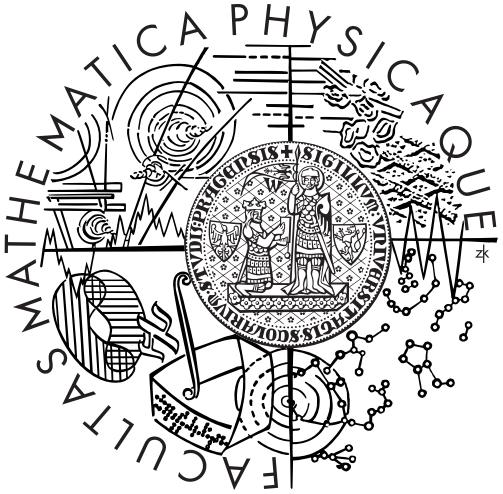

Jan Prokleška

Magnetoelastické jevy ve sloučeninách $Er(Co,X)_2$, X=p-element

Katedra fyziky elektronových struktur

Vedoucí práce: Prof. RNDr. Vladimír Sechovský, DrSc.

Studijní program: Fyzika kondenzovaných a makromolekulárních látek

In this place, I would like to say my best thanks to everyone, who supported me to raise this work and helped me in the whole study anyway.

First of all, I would like to thanks my supervisor Prof. Dr. Vladimír Sechovský for his guidance, for effective helps and support during my work and for introducing me into the area of magnetic studies.

I would like to express many thanks to Dr. Pavel Svoboda and Jana Vejpravová for their help and support in my work at laboratory, especially during the sample preparation.

I am very thankful to Doc. David Rafaja, Dr. Stanislav Daniš and Mgr. Milan Dopita for their help with my x–ray measurements and especially to Dr. Stanislav Daniš for measuring of the low temperature (He) x–ray data.

I would like to express thanks to Dr. Fuminori Honda for introducing me into the methods of thermal expansion measurements.

I would like to thank Ing. Josef Šebek, Dr. Eva Šantavá and Mgr. Blanka Janoušová for their help and introducing me into work with PPMS .

I would also express thanks to Doc. Martin Diviš for his help and patience during my understanding of theoretical concepts and background of magnetism.

Many thanks also belong to Ing. Miroslav Maryško for his help during my measurements on SQUID magnetometer.

I would like to thank Ing. Bendíková and Mgr. Uhlíř for making microprobe analysis.

Prohlašuji, že jsem svou diplomovou práci napsal samostatně a výhradně s použitím citovaných pramenů. Souhlasím se zapůjčováním práce.

V Praze dne 17. dubna 2003 Jan Prokleška

Contents

Název práce: **Magnetoelastické jevy ve sloučeninách $Er(Co,X)_2$, X=p–element**

Autor: Jan Prokleška

Katedra: Katedra fyziky elektronových struktur
Vedoucí diplomové práce: Prof. RNDr. Vladimír Sechovský, DrSc.
e-mail vedoucího: sech@mag.mff.cuni.cz

Abstakt: Sloučenina $ErCo_2$ patří ke skupině materiálů typu $RECo_2$ (RE – vzácná zemina), které přísluší ke kubickým Lavesovým fázím strukturního typu $MgCu_2$ (C15). V této práci byl studován vliv substitucí p kovem (3% zastoupení Al, Si, Ga, Ge, In v Co) na magnetické, transportní a magnetoelastické vlastnosti. U všech substitucí byl pozorován posun v teplotě fázového přechodu směrem k vyšším teplotám (od 43 K v případě Ga k 52 K pro In). Ve srovnání s chováním čistého $ErCo_2$ vykazuje materiál substituovaný In největší odlišnosti — teplota přechodu je posunuta z 33 K na 52 K, fázový přechod je na rozdíl od $ErCo_2$ druhého druhu a nebyl pozorován metamagnetický přechod nad T_C.

Klíčová slova: intermetalika vzácných zemin, magnetizace, magnetoresistivita, magnetoobjemové jevy

Title: **Magnetoelastic effects in $Er(Co,X)_2$ compounds, X=p–element**

Author: Jan Prokleška

Department: Department of electronic structures
Supervisor: Prof. RNDr. Vladimír Sechovský, DrSc.
Supervisor's e-mail address: sech@mag.mff.cuni.cz

Abstact: The $ErCo_2$ compound belong to a group of $RECo_2$ compounds (R – rare earth) crystallizing in the cubic Laves phase C15. The influence of substitution of p–element (3% of Al, Si, Ga, Ge, In in Co) on magnetic, transport and magnetoelastic properties was studied in this work. All substitutions shifts transition temperature to higher temperatures (from 43 K in the case of Ga to 52 K in the case of In). The In substitution shows the most different behavior in comparison to the data of pure $ErCo_2$ compound — transition temperature shifted from 33 K to 52 K, phase transition is of the second order contrary to pure $ErCo_2$ and no metamagnetic transition above T_C was observed.

Keywords: rare-earth intermetallics, magnetization, magnetoresistovity, magnetovolume effects

Chapter 1

Introduction

In recent years, Laves-phases rare-earth $RECo_2$ intermetallic compounds are subject of intensive studies, which can bring fundamental knowledge in a wide range of topics concerning the 4f localized and 3d itinerant magnetisms. The main reason for scientific interest is that the $RECo_2$ series meets well the requirements for a *true model multifunctional material* — many phenomena are determined mainly by one or two dominating microscope mechanism. This circumstance facilitates the interpretation of their physical properties by the use of general and simple theoretical models and makes such material a suitable testing object for different physical theories.

$ErCo_2$ is one of $RECo_2$ (RE = rare-eath metal) compounds, in which the Co magnetic moment emerges only at Curie temperature T_C when the Co 3d-electron band states become polarized owing to a huge molecular field caused by the ferromagnetically ordered 4f moments in the RE sublattice and a considerable RE-Co exchange interaction. The phenomenon, which happens in the Co sublattice at T_C, is in fact the itinerant 3d-electron metamagnetism. It is accompanied by dramatic anomalies in transport, cohesive and thermal properties, which give to the RCo_2–based materials a considerable application potential (magnetic refrigeration, device calibration etc.).

Some of these materials exhibit magnetic instability of the 3d-electron subsystem. The $RECo_2$ compounds are very sensitive to external magnetic field, pressure and changes of chemical surrounding of Co ions due to partial substitution Si, Al, Ga and other p–elements.

In order to separate and demonstrate the interplay among the different electronic subsystems (3d, 4d, 5d and 4f electrons), measurement of pseudobinary systems are performed, where either RE or Co is replaced by another element. In few cases, both RE and Co are simultaneously substituted. Although plausible explanation have been found for many effects observed in the $RECo_2$ Laves phases, not all of their properties are yet understood.

The aim of this work is to investigate the magnetism and related electronic properties of $ErCo_{1.94}X_{0.06}$ pseudobinary compounds. The experimental results focus on the influence of substitutions on the magnetic phase transition at T_C, the magnetovolume, magnetoresistance and magnetoelastic phenomena.

The outline of this work is following: Chapter 2 presents a brief theoretical description of the phenomena which are related to the studied compounds. In section 2.1, the two limiting models of magnetism (itinerant–electron and local–moment) are reviewed. In sections 2.2 and 2.3, basic models of exchange interactions (4f–3d exchange interaction, 3d magnetism and 4f–4f interaction) in $RECo_2$ compounds are described. The section 2.4 depicts the impact of magnetism on transport and elastic properties.

Chapter 3 gives general introduction to $RECo_2$ compounds. The previous study of magnetic and non–magnetic $RECo_2$ compounds is briefly discussed. Chapter 4 presents the experimental techniques and instruments, which were employed for the bulk measurements of the magnetic and electronic properties. In Chapter 5, experimental results observed on studied compounds are presented and their discussion is in Chapter 6. The concluding remarks of this thesis are summarized in Chapter 7. For clarity, most of graphs are presented in appendix A, the graphs included in the text are those, which are important or typical for discussed topic.

Chapter 2

General theory

2.1 Itinerant-electron and local-moment model

Magnetic properties of metallic materials can be understood in the framework of one of two approaches — itinerant electron model and the model in which localized magnetic moments are assumed. Both models can be used in fact only in limiting cases.

Local–moment model

Local–moment behavior is usually associated with the magnetic moments of well localized electrons, which do not contribute to conductivity or chemical bonding. Such situation is well established for most of the lanthanide–based compounds[1], as the 4f shell lies deeply inside the 5d and 6s shells. This leads to the unique situation that the electrons in a partially filled shell belong in fact to the chemically inert ionic core.

The model is based on spatially well defined electron wavefunctions, which are centred at particular ions. There is a negligible spatial overlap between 4f wavefunctions of neighbors which keep nearly the free–ion form. This leads to the well–defined energy levels in the solid which are only slightly modified with respect to the free–ion situation. Moreover, due to the fact that the wavefunctions are limited in space, the electrons have fully developed orbital moments (and accordingly the associated orbital magnetic moments). Probably the most transparent manifestation of the lo-

ion		$\frac{\mu_{\mathrm{eff}}}{\mu_{\mathrm{B}}}$	exp
La^{3+}	$4f^0$	0.00	dia
Ce^{3+}	$4f^1$	2.54	2.4
Pr^{3+}	$4f^2$	3.58	3.5
Nd^{3+}	$4f^3$	3.62	3.5
Pm^{3+}	$4f^4$	2.68	—
Sm^{3+}	$4f^5$	0.84	1.5
Eu^{3+}	$4f^6$	0.00	3.4
Gd^{3+}	$4f^7$	7.94	8.0
Tb^{3+}	$4f^8$	9.72	9.5
Dy^{3+}	$4f^9$	10.63	10.6
Ho^{3+}	$4f^{10}$	10.60	10.4
Er^{3+}	$4f^{11}$	9.59	9.5
Tm^{3+}	$4f^{12}$	7.57	7.3
Yb^{3+}	$4f^{13}$	4.54	4.5
Lu^{3+}	$4f^{14}$	0.00	dia

Table 2.1. Comparison of theoretical ($^{\mu_{\mathrm{eff}}}/_{\mu_{\mathrm{B}}} = g_{\mathcal{J}}\sqrt{J\,(J-1)}$) and experimental values of magnetic moments [31].

[1] with the exception of cerium, europium and ytterbium in some cases

ion		$g_J\sqrt{J(J-1)}$	$g_J\sqrt{S(S-1)}$	exp
K^+, La^{3+}	$3d^0$	0.00	0.00	dia
Ti^{3+}, V^{4+}	$3d^1$	1.55	1.73	1.7
V^{3+}	$3d^2$	1.63	2.83	2.8
V^{2+}, Cr^{3+}, Mn^{4+}	$3d^3$	0.77	3.87	3.8
Cr^{2+}, Mn^{3+}	$3d^4$	0.00	4.90	4.9
Mn^{2+} Fe^{3+}	$3d^5$	5.92	5.92	5.9
Fe^{2+}	$3d^6$	6.70	4.90	5.4
Co^{2+}	$3d^7$	6.64	3.87	4.8
Ni^{2+}	$3d^8$	5.59	2.83	3.2
Cu^{2+}	$3d^9$	3.55	1.73	1.9
Cu^+ Zn^{2+}	$3d^{10}$	0.00	0.00	dia

Table 2.2. Comparison of theoretical and experimental values of magnetic moments [39].

calized character of a system is that the observed intrinsic magnetic moments are close to full values expected from Hund's rules for a free ion (see table 2.1).

Local–moment model was firstly used for explanation of Curie law of paramagnetic susceptibility [36] and for derivation of Curie-Weiss law with additional hypothesis of molecular field [54].

Itinerant–electron model

The fundamental characteristics for the itinerant–electron model is strong overlap of the charge distributions of neighboring atoms, which can be found in compounds based on the 3d, 4d and 5d transitions metals (and light actinides), where the d (or 5f) electrons are largely delocalized and contribute to both conductivity and chemical bonding.

The electrons responsible for the magnetic moments originate from not completely filled shells in metals and are situated lower (in energy and space scale) than electrons forming conduction bands. In this case relatively wide bands are formed and populated according Pauli to exclusion principle. These electrons loose completely or nearly completely a non–zero time averaged angular momentum (and hence the orbital magnetic moment). The magnetism is mainly of spin origin with the presence of small orbital contribution due to the spin–orbit interaction (see table 2.2).

element	$\mathbf{N}(E_F)$	I_S
Li(bcc)	0.33	172
Be(fcc)	0.36	156
Ca(fcc)	10.5	74
Cr(bcc)	4.70	56
Mn(fcc)	10.5	60
Fe(bcc)	21	68
Co(fcc)	14	73
Ni(fcc)	27	74
Cu(fcc)	2	54
Zn(fcc)	2	76
Ga(fcc)	2.8	74
In(fcc)	3.4	30

Table 2.3. Stoner exchange integral I_S (in mRy) and density of states on Fermi energy $\mathbf{N}(E_F)$ (in Ry^{-1}) for some metallic elements [27], [18].

The effort to describe a metallic state started with the free electron gas model developed by Pauli [43]. After the development of the electron band model Bloch [8],

Mott [37] and Slater [48], [49] advanced the description of the metallic state as the electron gas, which was finalized by Stoner [50], [51], who succeeded to formulate a phenomenological "molecular field" model (analogous to the Weiss model) by employing the electronic bandstructure instead of the discrete angular momentum levels.

Stoner formulated model of itinerant electron magnetism on the following postulates:

- The carriers of magnetism are unsaturated spins in the d-band.
- Effects of the exchange are treated within the molecular field term.
- System must conform to Fermi statistic.

Under these assumptions the so called *Stoner criterion* for a spontaneous magnetic order of a system of itinerant electrons

$$I_{\mathrm{S}}\,\mathbf{N}(E_{\mathrm{F}}) > 1 \tag{2.1}$$

can be derived, where I_{S} is Stoner exchange integral and $\mathbf{N}(E_{\mathrm{F}})$ is density of states at the Fermi energy E_{F}. The values of $\mathbf{N}(E_{\mathrm{F}})$ and I_{S}, derived from the electronic band calculations [27] (using the KKR[2]–method and the LSDA[3] one for exchange and correlation) are in table 2.3 (bold elements fulfills the Stoner criterion (2.1)).

The criterion (2.1) can be looked into with the help of the following simple model (see fig. 2.1): To obtain a magnetic moment, we move electrons from a narrow zone (with bandwidth ΔE) near E_{F} from the majority to the minority band. To satisfy the Pauli principle they must be shifted to higher energies which causes an increase of kinetic energy ΔE_{k}.

On the other hand there is a drop in exchange energy ΔE_{xc} and the new (magnetic) configuration will be stable for $\Delta E_{\mathrm{k}} < \Delta E_{\mathrm{xc}}$. The change in kinetic energy is given by the number of moved electrons $\Delta N = \mathbf{N}(E_{\mathrm{F}})\Delta E$ multiplied by average energy change ΔE of one electron

$$\Delta E_{\mathrm{k}} = \mathbf{N}(E_{\mathrm{F}})\,(\Delta E)^2 \ . \tag{2.2}$$

The modification of exchange energy can be expressed as

$$\Delta E_{\mathrm{xc}} = I_{\mathrm{S}}\,M\,\Delta N = I_{\mathrm{S}}\,\mathbf{N}^2(E_{\mathrm{F}})\,(\Delta E)^2 \ , \tag{2.3}$$

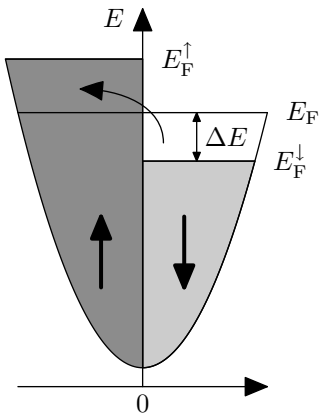

Figure 2.1. Spin split density of states. Fermi energy E_{F} for non–magnetic state and Fermi energies for spin–up $E_{\mathrm{F}}^{\uparrow}$ and spin––down $E_{\mathrm{F}}^{\downarrow}$ subbbands.

where M is the magnetization which is equal to the number of moved electrons, I_{S} is the Stoner exchange integral (effective interaction parameter), the term $I_{\mathrm{S}}M$ is the change of energy per one electron. When we use (2.2) and (2.3) in the stability condition $\Delta E_{\mathrm{k}} < \Delta E_{\mathrm{xc}}$ we get the Stoner criterion (2.1).

[2]Korringa–Kohn–Rostoker method [34], [33]
[3]local spin density approximation

The following types of magnetic materials can be distinguished considering the value of Stoner product $I_S \mathcal{N}(E_F)$:

- $I_S \mathcal{N}(E_F) < 1$ the compound is a *Pauli paramagnet*
- $I_S \mathcal{N}(E_F) - 1 \simeq 0^-$ the compound is close to onset of ferromagnetism and exhibits collective *metamagnetism*
- $I_S \mathcal{N}(E_F) - 1 \simeq 0^+$ the Stoner criterion is fulfilled but magnetization is small, the compound is called *very weak itinerant ferromagnet*
- for $I_S \mathcal{N}(E_F) > 1$ we have two possibilities:
  - two subbands with opposite spins are not filled, the compound is a *weak ferromagnet* (the case of Fe metal)
  - subband with lower energy is completely full, the compound is a *strong ferromagnet* (the case of Co and Ni metal)

Itinerant electron metamagnetism (IEMM)

The magnetic transition induced by a magnetic field from a low to a high magnetization state is called a metamagnetic transition. Various Co–based Laves phase compounds are good candidates for metamagnetic transition in intermetallic compounds (for example, the field induced transition in YCo_2 and $LuCo_2$ are typical examples of IEMM — see chap. 3, page 23). These compounds are exchange enhanced paramagnets due to the itinerant d electrons and they exhibits a maximum in the temperature dependence of susceptibility (the low field phenomenon) and a first–order field–induced phase transition from paramagnetic to ferromagnetic state was observed [24], [25]. The reason is ascribed to the Fermi level lying on a strong positive curvature of the density of states of these compounds where the Stoner criterion is almost fulfilled, thus the ferromagnetic state can be induced by the external magnetic field. This is called the itinerant electron metamagnetism.

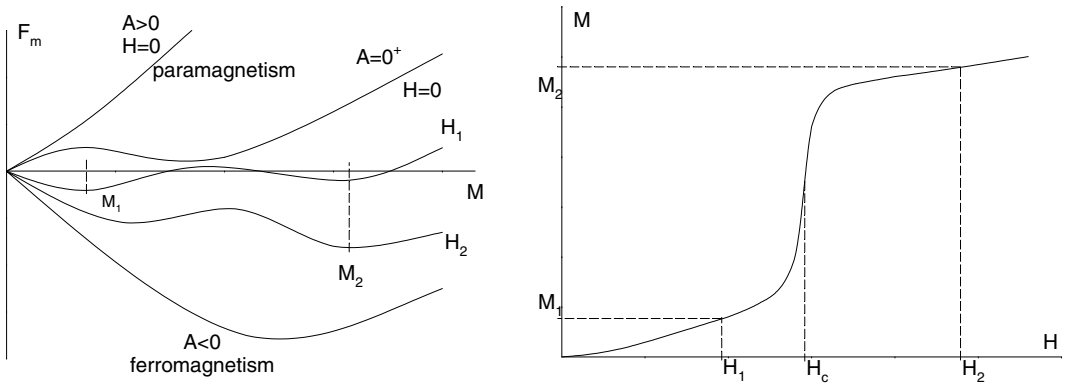

Figure 2.2. Dependency of magnetic states on the parameters of Landau expansion for magnetic free energy.

Existence of the IEMM can be understood with help of Landau expansion for d electron system in the case of the very weak itinerant ferromagnetism or the

exchange enhanced paramagnetism. Under this assumption, the magnetization is small enough and the molecular field approximation can be used. Using the Landau expansion of the magnetic free energy in the magnetization M of the d band

$$\Delta F_{\mathrm{m}}(M) = \frac{1}{2}A(T)M^2 + \frac{1}{4}B(T)M^4 + \frac{1}{6}C(T)M^6 \tag{2.4}$$

we can find the difference between the free energy of the ferromagnetic and the paramagnetic state. The coefficients $A(T)$ and $B(T)$ can be calculated in special cases [6], [57]. The dependence of the free energy on them is discussed below and is illustrated in fig. 2.2.
Discussion of parameters A, B from (2.4) in context of IEMM:

- The parameter A is positive, the compound is paramagnetic. The minimum of F_{m} lies at zero value of magnetization when $H = 0$.
- The parameter A is approximately zero but still positive. B is negative without external magnetic field, this leads to forming first minimum at $M \neq 0$, but the energy of this minimum is still larger than energy at $M = 0$ (see fig. 2.2), and the system becomes unstable. With applied field H_1, the negative minimum corresponding to the energy minimum appears at M_1 — see left part of fig. 2.2. In increasing magnetic field the dependency is changing, and at field H_2 (larger than a critical field H_{c}), the second minimum at M_2 becomes lower in energy than the first one. The first–order field induced transition (collective/itinerant electron metamagnetism) from a low to high magnetization state occurs.
- The parameter A is negative, the Stoner criterion is well fulfilled, the compound has a spontaneous magnetization and it is ferromagnetic.

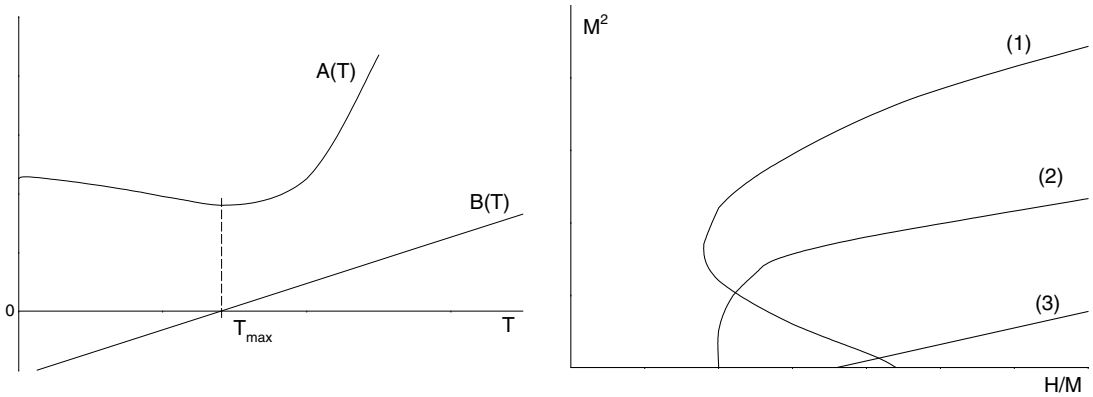

Figure 2.3. Schematic curves of temperature dependency of $A(T)$, $B(T)$ and Arrott plots. Curves (1), (2) and (3) corresponds to $T < T_{\max}$, $T = T_{\max}$ and $T > T_{\max}$ [57].

Based of the phenomenological theory it can be concluded [55] that the metamagnetism occurs if the susceptibility has a maximum value at the temperature $T_{\max}$. The temperature dependence of parameters $A(T)$ and $B(T)$ and its influence on $M(H)$ dependency in Arrott plot ([3], [4], [57]) is in figure 2.3.

More defined condition for appearance of metamagnetism can be found [47]:

$$A(T) > 0,\ B(T) < 0,\ C(T) > 0,\ \text{and}\ \frac{3}{16} < \frac{A(T)C(T)}{B(T)^2} < \frac{9}{20}\ ,$$

the $M(H)$[4] function is triple–valued function, hence hysteresis in magnetization curve is observed. When $A(T)C(T)/B(T)^2$ is smaller than $\frac{3}{16}$, the system is becomes ferromagnetic even at $H = 0$. On the other hand, when $A(T)C(T)/B(T)^2$ is larger than $\frac{9}{20}$, the metamagnetism does not occur at any H. At $\frac{A(T)C(T)}{B(T)^2} = \frac{9}{20}$, the equation $\partial H/\partial H = 0$ has an equal solution. In this case the hysteresis in a magnetization curve disappears.

2.2 Exchange interactions

The origin of the ordering of magnetic moments is in the exchange interaction. As a prototype an interaction that correlates spins in hydrogen molecule can be taken. These electrostatical interactions lead to a splitting of the energies of the symmetric and antisymmetric orbital and spin ($\uparrow\uparrow$, $\uparrow\downarrow$) states.

In figure 2.4, there are schematically reviewed three basic types of exchange interactions. If the magnetic atoms are nearest neighbors (so that overlap of relevant d or f orbitals is sufficient) the direct exchange can be effective. The best examples of direct exchange can be found in the ferromagnetic 3d metals Fe, Co and Ni.

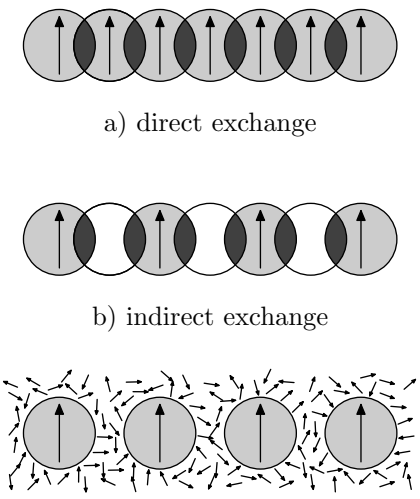

a) direct exchange

b) indirect exchange

c) indirect exchange - RKKY

Figure 2.4. Basic types of exchange interactions

In alloys and compounds, there are ions carrying magnetic moments frequently separated by other atoms, which can yield various types of indirect exchange interactions. The indirect exchange (super–exchange) is typical for materials in which the magnetic atoms are surrounded by ligands that do not carry permanent magnetic moments. This interaction is specific for RET_2 compounds although it was introduced to describe a situation in magnetic oxides.

The weak RKKY[5] interaction between two magnetic atoms is mediated by the conduction electrons polarized in the vicinity of magnetic ion (Fig. 2.4 c). The RKKY interaction plays an important role in the intermetallic compounds.

Generally, the exchange interaction energy between two magnetic ions can be described as[6]

$$\mathcal{H}_{ij}^{\mathrm{ex}} = -2\mathbf{J}_{ij}\mathcal{S}_i\mathcal{S}_j\ , \tag{2.5}$$

[4] obtained from $H = \frac{\mathrm{d}\Delta F}{\mathrm{d}M}$

[5] Named after Ruderman, Kittel, Kasuya and Yosida who have developed relevant model ([45], [29] and [58]).

[6] In the case of lanthanides and actinides we use expression $\mathcal{H}_{ij}^{\mathrm{ex}} = -2\boldsymbol{J}_{ij}(g_\mathcal{J} - 1)^2\boldsymbol{\mathcal{J}}_i\boldsymbol{\mathcal{J}}_j$, where $g_\mathcal{J}$ is Landé factor given by (2.14) and $\boldsymbol{\mathcal{J}}_k$ is total momentum of k th ion

where $\mathbf{J}_{ij}$ is the exchange integral ($10^2 - 10^3$ K for direct exchange in 3d metals, $10^0 - 10^2$ K for indirect exchange), and $\mathbf{S}_k$ is spin operator belonging to the kth atom. The exchange energy contribution from the whole system can be obtained by summation of (2.5) through all pairs in system

$$\mathcal{H}^{\mathrm{ex}} = -\sum_{i \neq j} \mathbf{J}_{ij} \mathbf{S}_i \mathbf{S}_j \ .$$

This can be rewritten in the term of molecular (mean, Weiss [54]) field H_{m}

$$\begin{aligned} \mathcal{H}^{\mathrm{ex}} &= -\sum_{i \neq j} \mathbf{J}_{ij} \mathbf{S}_i \mathbf{S}_j = -\sum_i \underbrace{g_i \mu_{\mathrm{B}} \mathbf{S}_i}_{\mu_i} \sum_{i \neq j} \underbrace{\frac{\mathbf{J}_{ij}}{g_i g_j \mu_{\mathrm{B}}^2}}_{V_{ij}} \underbrace{\mu_{\mathrm{B}} g_j \mathbf{S}_j}_{\mu_j} = \\ &= -\sum_i \mu_i \sum_{i \neq j} V_{ij} \mu_j = -\sum_i \mu_i H_{\mathrm{m}} \ . \end{aligned}$$

2.3 Magnetic interactions in $RECo_2$

Magnetic interactions in $RECo_2$ compounds are interesting as the rare earth metal has a well–defined magnetic moment, while 3d electron states form an energy band.

The strongest interaction in this system is 4f–3d (RE–Co). This interaction governs magnetic and transport properties of this compounds. Since the 4f shell of the rare–earth ion is deeply embedded inside, this interaction is indirect and is mediated by the conduction electron states (5d – mainly, 6s) of the RE ion.

Another interactions are 3d–3d (Co–Co) and indirect 4f–4f (RE–RE) of RKKY type which is weakest but has a long range character and is mediated by the conduction electrons.

At T_{C}, the 4f moments are ferromagnetically ordered and a strong molecular field from the 4f sublattice acts on the 3d itinerant states, which leads to an induced Co moment of about $1\mu_{\mathrm{B}}$ [38] for heavy $RECo_2$ compounds.

4f–4f interaction (RKKY model)

Since the 4f shells lies deeply inside the outer closed shells of the atom, the 4f–4f interaction is indirect. The RKKY model describes the 4f–4f interaction as mediated by conduction electrons[7]. It's usually described in the way that 4f moment localized on the ion i interacts with conduction electrons, leading to their spin polarization. The spin polarized electrons interacts with another 4f spin localized on the ion j and therefore creates an indirect interaction between the 4f spins $\mathbf{S}_i$ and $\mathbf{S}_j$.

3d–3d interaction (basics of the band theory)

The 3d band calculation is well treated in the Hartree-Fock approximation based on the assumption that each electron is placed in the electrostatic potential of metal

[7] The situation becomes more complex in the case of $RECo_2$ compounds — the interaction may be also mediated by the 3d itinerant electrons.

which is taken as a sum of atomic potentials V_i centering on the various lattice sites $i \Rightarrow V \approx \sum V_i$. Therefore the Hamiltonian describing the interaction of d electrons in metal environment can be written as $\mathcal{H} = T + \sum V_i$, where the former term is the kinetic energy of an electron and the second one is the electrostatical potential of metal. This problem is solved by means of LCAO[8] method, where the wave functions $|\Psi\rangle$ are taken as linear combinations of atomic orbitals $|\Psi\rangle = \sum a_{im}|i\ m\rangle$, where constant a_{im} fulfills the orthonormality condition $\sum |a_{im}|^2 = 1$ and m is the projection of the angular moment. The energy of the d band can be determined as

$$\left(T + \sum V_i\right)\Big|\Psi\Big\rangle = E|\Psi\rangle$$

and the energy change from the atomic state to the metal is calculated as

$$\begin{aligned} E &= \sum_{im} |a_{im}|^2 \alpha_{im} + \sum_{ijmm'} a^*_{im} a_{jm'} \beta_{ijmm'} \ , \\ \alpha_{im} &= \Big\langle im \Big| \sum V_j \Big| \, im \Big\rangle \ , \\ \beta_{ijmm'} &= \langle im \, |V_j| \, jm' \rangle \ . \end{aligned}$$

The atomic states $|im\rangle$ still remain under the influence of $\sum V_i$, thus the α term is only to shift of the energy of atomic levels. In the β term the atom states are changed from $|im\rangle$ to $|jm'\rangle$, thus integrals β are called transfer integrals, mixing the atomic states into molecular states extending over the whole crystal.

The character of the 3d band depends strongly on the Co–Co atomic spacing $d_{\mathrm{Co-Co}}$; it becomes narrower when increasing the spacing between the atoms.

4f–3d interaction — simple model of electronic structure ($3d_{Co}$—$5d_{RE}$ mixing)

The 3d Co–band and 5d RE–band hybridize, yielding to bonding — antibonding band structure[9] (analogue to bonding — antibonding levels in $RECo_2$ molecule — see fig. 2.5). In the free atoms, the energy of the Co 3d states lies lower then that of RE 5d states (see fig. 2.5 a), thus the bonding band will obviously be dominated by 3d states, while the antibonding band has mainly 5d character. The degree of mixing between the 3d and 5d states depends on the overlap matrix element and on the energy separation between the 3d and 5d bands. If this energy separation is increased, the mixing will decrease and the opposite holds when the separation is decreased.

Now we introduced the effects due to the 4f states, which retain their atomic character in the solid (and their energy location[10] (relative to the 5d and 3d state energies) is not important). When the 4f electrons remain localized in the core of RE ion, they will influence the magnetic properties of valence electrons through the

[8] **L**inear **C**ombination of **A**tomic **O**rbital [26]

[9] In reality there is generally no such clear separation in energy between these two parts of electronic structure, but it is used in this model for clarity.

[10] Except some cerium compounds where the energy position of 4f state is located in the gap between bonding and antibonding states.

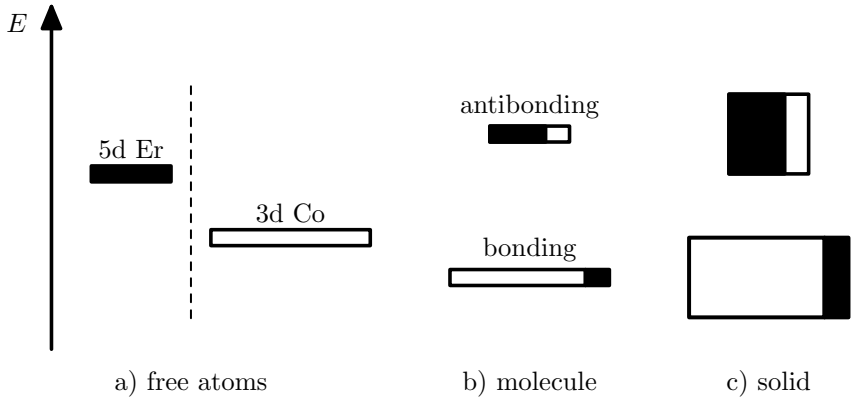

Figure 2.5. Schematic representation of the relative position between 5d and 3d atomic levels (a), bonding and antibonding levels for $RECo_2$ molecule (b) and illustration of their broadening in a solid (c). The amount of mixing between the original 3d and 5d states is illustrated by the black and white areas. (After [10].)

exchange potential. Since the 4f wave function has limited extension, this coupling will take place essentially within the rare–earth ion and mainly with the lanthanide 5d electrons (which have larger density and overlap with the 4f states than have the 5p or 5s states). The local exchange interactions are positive and the 4f and 5d spins will align parallel and the strength of the coupling will clearly be dependent upon the number of unpaired 4f spins. By reason that the 5d states are hybridized with the 3d states the 4f spin moments couple indirectly to the 3d spin moments.

If we assume that the 3d electrons spin–polarize, then the energy densities from fig. 2.5 c) are modified as illustrated in fig. 2.6. The energy separation between bonding and antibonding subbands becomes different for the two spin directions, therefore the 3d—5d hybridization is different for majority and minority spins. Therefore now a decrease of its 5d content yields for the majority bonding band. This has the effect that the spin-up (majority) occupation of the 5d part becomes less than the spin-down (minority) occupation of the 5d part. Thus there is a total spin-down 5d moment on the rare-earth atom.

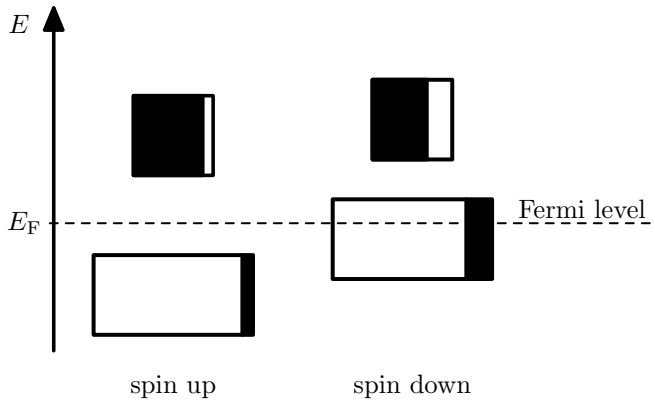

Figure 2.6. Spin–up (majority) and spin–down (minority) densities of states for a saturated ferromagnetic state. The amount of hybridization between 3d and 5d states becomes different for the two spin directions (illustrated by the black and white areas).(After [10].)

As stated in the 3rd Hund rule, the 3d cobalt moments are aligned antiparallel to the 4f moment in the heavy rare–earth $RECo_2$ and parallel in the light rare-earth

$RECo_2$ compounds.

Sublattice model

The effect of the 4f-3d exchange interaction can be described by the two sublattice model [9], in which $RECo_2$ crystal is consider as consisting of two intergrown sublattices — the RE sublattice (4f localized moments) and the Co sublattice (itinerant 3d electrons yielding exchange enhanced paramagnetism). We suppose, that these sublattices have magnetizations M_{RE} and M_{Co}, respectively. In an applied external field H, the magnetization M_{RE} and M_{Co} above T_{C} can be expressed as

$$M_{\mathrm{RE}} = \frac{C_{\mathrm{RE}}}{T}\Big(H + \upsilon_{\mathrm{RE-RE}} M_{\mathrm{RE}} + \upsilon_{\mathrm{RE-Co}} M_{\mathrm{Co}}\Big) \ , \tag{2.6}$$

$$M_{\mathrm{Co}} = \chi^0_{\mathrm{Co}}\Big(H + \upsilon_{\mathrm{Co-Co}} M_{\mathrm{Co}} + \upsilon_{\mathrm{RE-Co}} M_{\mathrm{RE}}\Big) \ , \tag{2.7}$$

where χ^0_{Co} is the paramagnetic susceptibility of Co sublattice, C_{RE} is the Curie constant of the rare–earth atoms, the $\upsilon_{\mathrm{RE-RE}}$, $\upsilon_{\mathrm{Co-Co}}$ and $\upsilon_{\mathrm{Co-RE}}$ are the molecular field coefficients which represent exchange interactions inside rare–earth and cobalt sublattices and between them, respectively. For evaluation of $\chi = \chi_{\mathrm{RE}} + \chi_{\mathrm{Co}}$ we rewrite (2.7) into

$$\chi_{\mathrm{Co}} = \frac{\chi^0_{\mathrm{Co}}}{1 - \chi^0_{\mathrm{Co}}\upsilon_{\mathrm{Co-Co}}}(1 + \upsilon_{\mathrm{RE-Co}}\chi_{\mathrm{RE}}) = \chi_{\mathrm{ee}}(1 + \upsilon_{\mathrm{RE-Co}}\chi_{\mathrm{RE}}) \ , \tag{2.8}$$

where χ_{ee} is the exchange-enhanced susceptibility (susceptibility of the pure cobalt sublattice — $\chi_{\mathrm{RE}} = 0$). Then χ we be written as $\chi = \chi_{\mathrm{RE}} + \chi_{\mathrm{ee}}(1 + \upsilon_{\mathrm{RE-Co}}\chi_{\mathrm{RE}}) = \chi_{\mathrm{ee}} + {} + (1 + \upsilon_{\mathrm{RE-Co}}\chi_{\mathrm{ee}})\chi_{\mathrm{RE}}$, where χ_{RE} can be derived from (2.6) and (2.8) as

$$\chi_{\mathrm{RE}} = \frac{1 + \upsilon_{\mathrm{RE-Co}}\chi_{\mathrm{ee}}}{\frac{T}{C_{\mathrm{RE}}} - \upsilon_{\mathrm{RE-RE}} - \upsilon^2_{\mathrm{RE-Co}}\chi_{\mathrm{ee}}} \ .$$

Finally, for χ we get the *modified Curie–Weiss law*

$$\chi = \frac{C'}{T - \Theta'_{\mathrm{p}}} + \chi_{\mathrm{ee}} \ , \tag{2.9}$$

where

$$C' = C_{\mathrm{RE}}(1 + \upsilon_{\mathrm{RE-Co}}\chi_{\mathrm{ee}})^2 \ , \tag{2.10}$$

$$\Theta'_{\mathrm{p}} = (\upsilon_{\mathrm{RE-RE}} + \upsilon^2_{\mathrm{RE-Co}}\chi_{\mathrm{ee}})C_{\mathrm{RE}} \ . \tag{2.11}$$

The values of $\upsilon_{\mathrm{RE-Co}}$ and $\upsilon_{\mathrm{RE-RE}}$ can be deduced from these equations. Sometimes[11] it's more convenient to considered the spin independent exchange–interaction coefficients $J_{\mathrm{RE-Co}}$ and $J_{\mathrm{RE-RE}}$. Their values are given by

$$J_{\mathrm{RE-Co}} = \frac{g_{\mathcal{J}}\upsilon_{\mathrm{RE-Co}}}{g_{\mathcal{J}} - 1} \ , \tag{2.12}$$

$$J_{\mathrm{RE-RE}} = \frac{g^2_{\mathcal{J}}\upsilon_{\mathrm{RE-RE}}}{2\,(g_{\mathcal{J}} - 1)^2} \ , \tag{2.13}$$

[11] for comparing interactions in compounds with different RE atoms

where $g_{\mathcal{J}}$ is Landé factor[12]

$$g_{\mathcal{J}} = 1 + \frac{J(J+1) + S(S+1) - L(L+1)}{2J(J+1)} \ . \tag{2.14}$$

2.4 Impact of magnetism on transport and elastic properties

Transport properties

Transport phenomena include electrical and thermal resistivity, thermopower, magnetoresistivity and the Hall effect. These are the physical properties of solids dealing with a charge or heat transport under the influence of external forces. This can be in general described[13] as

$$J_i = \sum_{j=1}^{n} L_{ij} X_j \ ,$$

where $\mathbf{J}$ is current (response of the system), $\mathbf{X}$ is generalized external force and L_{ij} are so–called linear transport coefficients. The simultaneous application of an external magnetic field is a further scenario — the magnetic field does not cause a drift velocity within a conduction system, but it has an influence on the conduction electron trajectories and thus influence the charge current.

The most common approach to describe transport phenomena is the Boltzmann formalism, which is based on the assumption that the distribution function in the phase space $(\mathbf{r}, \mathbf{k})$ can be defined. From this distribution function f we can calculate appropriate current densities [41]. The distribution function is a solution of Boltzmann equation (which describes time development of the distribution function) in the presence of external forces $\mathbf{F}$

$$\frac{\partial f(\gamma, \mathbf{r}, t)}{\partial t} + \frac{1}{\hbar}\mathbf{F} \cdot \nabla_k f(\gamma, \mathbf{r}, t) + \mathbf{v} \cdot \nabla_r f(\gamma, \mathbf{r}, t) = \left(\frac{\partial f(\gamma, \mathbf{r}, t)}{t}\right)_{\text{collision}} \ , \tag{2.15}$$

where γ is an abbreviation for band quantum numbers n, σ and $\mathbf{k}$ ($\gamma = (n\ \sigma\ \mathbf{k})$) and $\mathbf{v}$ is the velocity of a wave packet. Left hand side of (2.15) describes the time development of the distribution function caused by the semiclassical equations of motion

$$v = \frac{\mathrm{d}\mathbf{r}}{\mathrm{d}t} = \frac{1}{\hbar}\nabla_k E_{n\sigma}(\mathbf{k}) \ ,$$
$$\frac{\mathrm{d}\mathbf{k}}{\mathrm{d}t} = \frac{1}{\hbar}\mathbf{F} \ .$$

The right hand side is the collision term, which takes into account the changes of the distribution function due to scattering processes.

[12] It should be noted, that in the case $RECo_2$ compounds, the T_C is proportional to the de Gennes factor $(g_{\mathcal{J}} - 1)^2 J(J+1)$.

[13] under the condition of linearity between the forces $\boldsymbol{X}$ and currents $\boldsymbol{J}$

In the presence of time–independent electric and magnetic field applied to the system of conduction electrons, the external force $\mathbf{F}$ is the Lorenz force

$$\mathbf{F} = -e\left(\frac{1}{c}\mathbf{v}\times\mathbf{B}+\mathbf{E}\right) \ .$$

For this time–independent distribution function we are looking for time–independent solution of Boltzmann equation (2.15) for distribution function $f(\gamma,\mathbf{r})$

$$-\frac{e}{\hbar c}\left(\mathbf{v}_\gamma\times\mathbf{B}\right)\cdot\nabla_k f(\gamma,\mathbf{r}) - \frac{e}{\hbar}\mathbf{E}\cdot\nabla_k f(\gamma,\mathbf{r}) + \mathbf{v}_\gamma\cdot\nabla_r f(\gamma,\mathbf{r}) = \left(\frac{\partial f(\gamma,\mathbf{r},t)}{t}\right)_{\text{collision}} \ .$$

Resistivity

Under assumption of independency of scattering mechanisms, we can use the so–called *Matthiessen's rule* for the description of resistivity. The resistivity can be then written in general as

$$\varrho_{\text{tot}} = \varrho_0 + \varrho_{\text{ph}} + \varrho_{\text{mag}} \ , \tag{2.16}$$

where the subscripts denote the residual resistivity, the resistivity owing to phonon scattering and the resistivity owing to the spin-dependent resistivity.

The residual resistivity is given by the impurity scattering and is temperature independent. In the ideal case (nonmagnetic, single crystal sample) ϱ_0 is much smaller than other terms (except at lowest temperature).

The phonon term ϱ_{ph} comes from the electron–phonon scattering. Under the presumption, that the conduction electrons are part of the one and the same s–conduction band and they are scattered into vacant states within the same band, the $\varrho_{\text{ph}}(T)$ dependence can be approximated by the *Bloch-Grüneisen law*, derived using the Debye model

$$\varrho_{\text{ph}}(T) = 4R_\Theta\left(\frac{T}{\Theta}\right)^5\int_0^{\frac{\Theta}{T}}\frac{x^5\mathrm{d}x}{\left(\mathrm{e}^x-1\right)\left(1-\mathrm{e}^{-x}\right)} \ , \tag{2.17}$$

where Θ is the Debye temperature of the material and R_Θ includes, among other fundamental physical quantities, the electron–phonon coupling constant and is proportional to the phonon part of resistivity at the Debye temperature. For the high and the low temperature region it can be derived from (2.17) that

$$\begin{aligned}\varrho_{\text{ph}}(T) &\propto T^5 \quad \text{for} \quad T \ll \Theta \ ,\\ \varrho_{\text{ph}}(T) &\propto T \quad \text{for} \quad T \gg \Theta \ ,\end{aligned}$$

respectively.

The third term in (2.16) describes the spin–dependent scattering phenomena. In paramagnetic region ϱ_{mag} is temperature independent and proportional to the de Gennes factor (the so–called spin–disorder resistivity)

$$\varrho_{\text{spd}} = \frac{3\pi^2 N m^*}{he^2E_{\text{F}}}\left|\mathfrak{J}\right|^2\left(g-1\right)^2 J(J+1) \ ,$$

where $\mathfrak{J}$ is a coupling constant of the electron–spin interaction.

Below the magnetic ordering temperature in the magnetically ordered state the temperature dependence of the magnetic part of resistivity critically depends on the details of the magnetic ordering and on the dispersion of the quasiparticles (magnons etc.) involved in the interaction with conduction electrons. For instance, in the non–gapped dispersion relation of ferromagnetic magnons the electrical resistivity varies as T^2 at low temperatures $T \ll T_{\mathrm{C}}$ (in antiferromagnetic compounds as T^4 for $T \ll T_{\mathrm{N}}$). In the case of a presence of a gap Δ in the dispersion relation, the electrical resistivity can be described as [1]

$$\varrho_{\mathrm{mag}} = AT^2 + ET\left(1 + 2\frac{T}{\Delta}\right)\mathrm{e}^{-\frac{\Delta}{T}} \ ,$$

where E depends on the spin–disorder resistivity and on the electron–magnon coupling constant.

Magnetoresistivity

Under the influence of a magnetic field we have to consider the conductivity (resistivity) as a tensor and Ohm's law is written as

$$\mathbf{i} = \boldsymbol{\sigma}(T, \mathbf{B})\mathbf{E} \ ,$$

where $\mathbf{i}$ is electrical current density, $\mathbf{E}$ is the electric field and $\boldsymbol{\sigma}$ is the temperature and field dependent conductivity tensor[14]. The conductivity tensor $\boldsymbol{\sigma}$ for an isotropic (cubic) material in the presence of $\mathbf{B} = (0, 0, B)$ is given as

$$\boldsymbol{\sigma}(B) = \begin{pmatrix} \sigma_{xx}(B) & \sigma_{xy}(B) & 0 \\ -\sigma_{xy}(B) & \sigma_{yy}(B) & 0 \\ 0 & 0 & \sigma_{zz}(B) \end{pmatrix}$$

and the corresponding resistivity tensor $\boldsymbol{\varrho}$

$$\boldsymbol{\varrho}(B) = \begin{pmatrix} \varrho_{\perp}(B) & \varrho_{\mathrm{H}}(B) & 0 \\ -\varrho_{\mathrm{H}}(B) & \varrho_{\perp}(B) & 0 \\ 0 & 0 & \varrho_{\parallel}(B) \end{pmatrix} \ ,$$

where $\varrho_{\perp}$ and $\varrho_{\parallel}$ are resistivities in transverse and longitudinal external magnetic field and ϱ_{H} is the Hall resistivity, respectively. The transverse and longitudinal magnetoresistance are defined by

$$\frac{\Delta\varrho_{\perp}}{\varrho} = \frac{\varrho_{\perp}(T, B) - \varrho(T, B = 0)}{\varrho(T, B = 0)}$$

and

$$\frac{\Delta\varrho_{\parallel}}{\varrho} = \frac{\varrho_{\parallel}(T, B) - \varrho(T, B = 0)}{\varrho(T, B = 0)} \ ,$$

respectively.

[14] In the absence of an external magnetic field the conductivity becomes a scalar for cubic symmetry — $\mathbf{i} = \sigma(T, \mathbf{B})\mathbf{E}$. In an applied field the symmetry is broken, but the Onsager relationships still hold $\sigma_{ij}(\mathbf{B}) = \sigma_{ji}(-\mathbf{B})$.

Elastic properties

The linear thermal expansion is defined as

$$\frac{\Delta l(T)}{l} = \frac{l(T) - l(T_0)}{l(T_0)} \approx \frac{1}{3}\frac{V(T) - V(T_0)}{V(T_0)} = \frac{1}{3}\omega_\mathrm{s} \ ,$$

where T_0 is the reference temperature to which the data are normalized.

The magnetovolume effect ω_s and the magnetic moment μ for a single sublattice ferromagnet are connected by a following phenomenological expression [2]

$$\omega_\mathrm{s} = kC\mu^2 = n\mu^2 \ ,$$

where k is the compressibility, C is the magnetoelastic–coupling constant. The magnetoelastic–coupling coefficient $n = kC$ is used when the k and C factors cannot be found separately.

In paramagnetic region, linear thermal expansion can be described as a sum of phononic, electronic and magnetoelastic part [21]

$$\left(\frac{\Delta l(T)}{l}\right)_\mathrm{tot} = \left(\frac{\Delta l(T)}{l}\right)_\mathrm{ph} + \left(\frac{\Delta l(T)}{l}\right)_\mathrm{el} + \left(\frac{\Delta l(T)}{l}\right)_\mathrm{mag} \ . \tag{2.18}$$

The temperature variation of these contributions can be described in a following way [7]

$$\left(\frac{\Delta l(T)}{l}\right)_\mathrm{el} = K_1 T^2 \ , \tag{2.19}$$

$$\left(\frac{\Delta l(T)}{l}\right)_\mathrm{ph} = K_2 \, \frac{T^4}{\Theta^3} \int_0^{\frac{\Theta}{T}} \frac{x^3 \mathrm{d}x}{\mathrm{e}^x - 1} \ . \tag{2.20}$$

The temperature dependence of the magnetoelastic part is in the presence of spin fluctuations given as

$$\left(\frac{\Delta l(T)}{l}\right)_\mathrm{mag} = K_1' T^2 \tag{2.21}$$

(at low temperatures, [57]). From (2.18)–(2.21) we get

$$\left(\frac{\Delta l(T)}{l}\right)_\mathrm{tot} = \left(K_1 + K_1'\right) T^2 + K_2 \, \frac{T^4}{\Theta^3} \int_0^{\frac{\Theta}{T}} \frac{x^3 \mathrm{d}x}{\mathrm{e}^x - 1} \ . \tag{2.22}$$

Chapter 3

Physics of $RECo_2$ materials

Ordered metallic alloys with a well defined crystal structure are classified as intermetallic compounds, or intermetallics. Due to the metallic character of bonding, the crystal structures of intermetallics tend to reach the highest symmetry, highest space filling and highest coordination number.

The RE–3d intermetallics are the ordered alloys of rare–earth (RE) and 3d–transition elements (T) and can involve one or both elements with magnetic moments. These compounds exist in a relatively narrow compositional range, and RE and T atoms are distributed at proper and definite positions in the crystallographic cell. Accordingly, two magnetic sublattices (f– and d–electron subsystem) can be distinguished in the RE–3d intermetalics. While the number of pure magnetic 3d– and 4f–elements is about 20, there are several hundreds of binary RE–3d intermetallics and thousands among the ternary RE–3d–M systems.

3.1 $RECo_2$ compounds generally

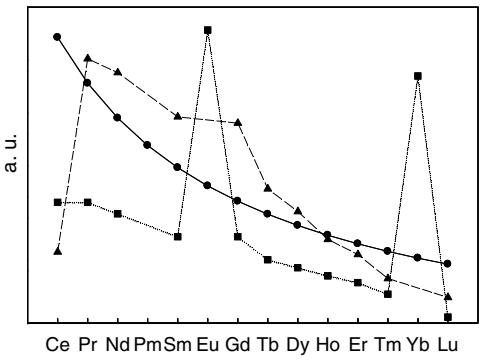

Figure 3.1. Theoretical atomic radii (•), radii of metallic binding (■) and lattice parameters of $RECo_2$ (▲) (data from [2], [11], [14], [30] and [46])

The $RECo_2$ compounds crystallize in the $MgCu_2$–type (C15) structure (space group Fd3m), where the RE atoms form a diamond lattice and the remaining space inside the cell is occupied by regular tetrahedra consisting of the Co atoms (see figure 3.2). In this structure, the RE and Co atoms each occupy one crystallographic site, namely the $8a$ and $16b$ sites, respectively. The ionic radii ratio among the $RECo_2$ series (r_{RE}/r_{Co}) varies between 1.26 and 1.24, i.e. it is on average larger then the ideal ratio ($r_{RE}/r_{Co} = 1.225$) for the most dense packed lattice. It can been shown [21] that this ratio is not the only parameter, which is responsible for the stability of the

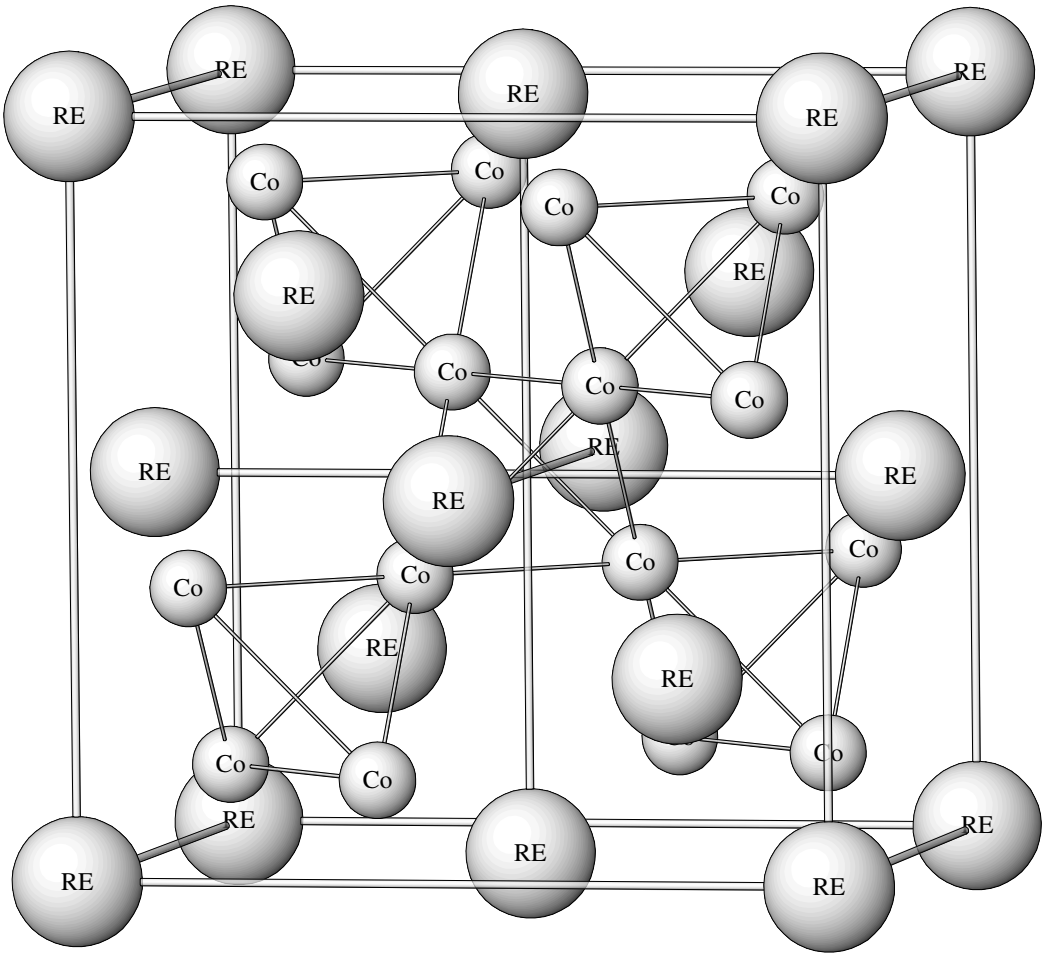

Figure 3.2. Crystal structure of $RECo_2$ compounds (cubic Laves phase C15).

C15 structure — the crystal structure of the RE–3d intermetallic is determined by the conduction electron concentration, too.

The lattice parameters of an isostructural series of rare–earth intermetallics smoothly decrease from lanthanum to lutetium. This is attributed to the so–called *lanthanide contraction* [17], [32] and ascribed to the fact that though the electron count of the 4f shell increases, it cannot completely screen the increase in the nuclear charge and, therefore, the outer electrons become constricted. However, compounds with cerium, samarium, europium, thulium, or ytterbium may significantly deviate from this simple dependence since their valency can be bigger or smaller than 3^+, thus cause a decrease or an increase of the unit cell volume, respectively (see fig. 3.1).

In order to separate and demonstrate the interplay among the different electronic subsystems (3d, 4d, 5d and 4f electrons), pseudobinary systems are investigated, where either RE or Co is replaced by another element. In few cases both, RE and Co are simultaneously substituted. Although for many effects observed in the $RECo_2$ Laves phases a plausible explanation have been found, not all of their properties are yet understood.

3.2 Nonmagnetic compounds

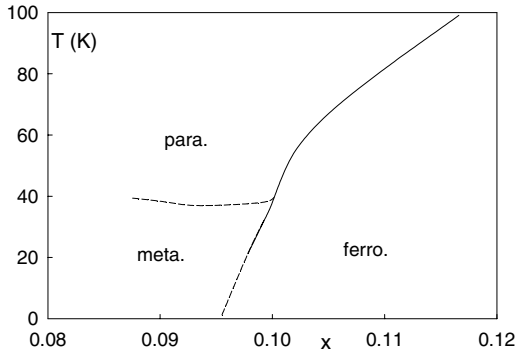

Figure 3.3. Magnetic phase diagram of $Lu(Co_{1-x}Ga_x)_2$ for low concentration [16].

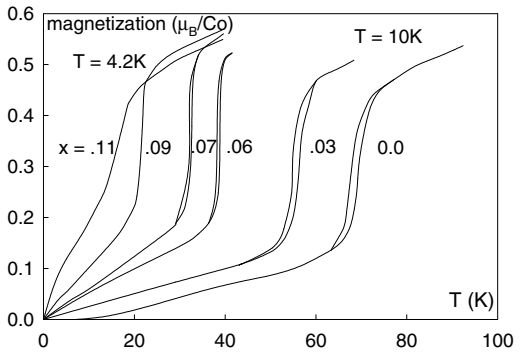

Figure 3.4. Low temperature magnetization process of $Y(Co_{1-x}Al_x)_2$ [25].

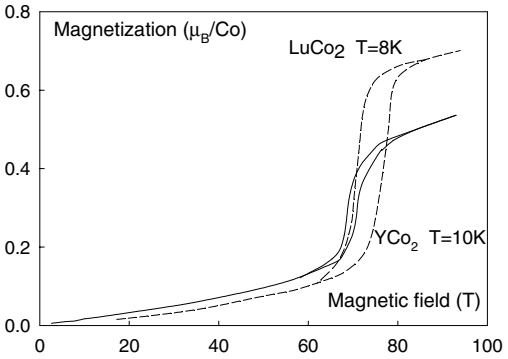

Figure 3.5. Metamagnetic transitions in $LuCo_2$ and YCo_2 [25].

Among the RE–3d cubic Laves phases the magnetism of the 3d partner is most strongly influenced by the magnetic RE sublattice in the $RECo_2$ series. Within this series, $ScCo_2$, YCo_2 and $LuCo_2$ are nonmagnetic, however, they show features characteristic for exchange enhanced Pauli paramagnetism (and exhibit metamagnetic phase transition to the ferromagnetic state in high fields). The driving mechanism, which determines the magnetic properties of these compounds, rests upon an interplay (hybridization) of the Co 3d– and the outside rare–earth d–wave functions (3d–5d in $LuCo_2$, 3d–4d in YCo_2 and 3d–3d in $ScCo_2$). In absence of an internal molecular field, the hybridization is expected to be the dominant factor forming most of the physical properties of $RECo_2$ compounds (not only with not magnetic RE). The hybridization is also important (in relation to IEMM) in the paramagnetic state of the $RECo_2$ compounds with magnetic RE elements.

The values of critical field H_c for the IEMM were estimated [56] from calculated magnetization in a ground state as a function of magnetic field for $ScCo_2$ (120 T), YCo_2 (89 T) and $LuCo_2$ (94 T). Measurements in pulsed high magnetic fields [24], [25] revealed sharp metamagnetic transitions in compounds YCo_2 (at 69 T) and $LuCo_2$ (74 T) (see figure 3.5), but no transition up to 120 T in the case $ScCo_2$.

The metamagnetic transition is influenced by a position of the Fermi level (E_F), which can be modified by a substitution for Co by a small amount of Fe or Ni. The iron substitution shifts E_F to the lower energy side, while the nickel substitution has the opposite effect. The H_c shift is linear for small substitutions $\sim +7.2\,\mathrm{T}/\%$

for Ni substitution and $-4.5\,\mathrm{T}/\%$ for Fe substitution. In the case of simultaneous substitutions ($YCo_{1.96}Fe_{0.02}Ni_{0.02}$ (2% subst.)) there is a small increase of 2 T in H_c [25].

By replacing Co by another element (Al, Ga), a significant reduction in H_c (to several tesla) and the onset of weak ferromagnetism have been observed (for an example see figures 3.3 and 3.4).

When a nonmagnetic RE atom in $RECo_2$ is replaced with a magnetic one, the Co moment is induced by the effective field from the RE site. The effective field can be evaluated using the relation $B_{\mathrm{eff}}\ (\mathrm{T}) = 84(g_{\mathcal{J}} - 1)J$, where $g_{\mathcal{J}}$ is the g–factor of RE and J is a total angular momentum [23]. The induced Co moment is found to increase rapidly at about 70 T, indicating that the effective field produces metamagnetic transition. This value corresponds to the critical field of YCo_2.

3.3 Magnetic compounds

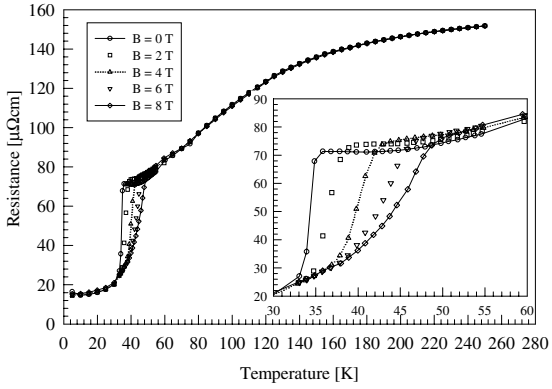

Figure 3.7. Temperature dependency of electrical resistivity of $ErCo_2$ in magnetic fields. (Figure from [15].)

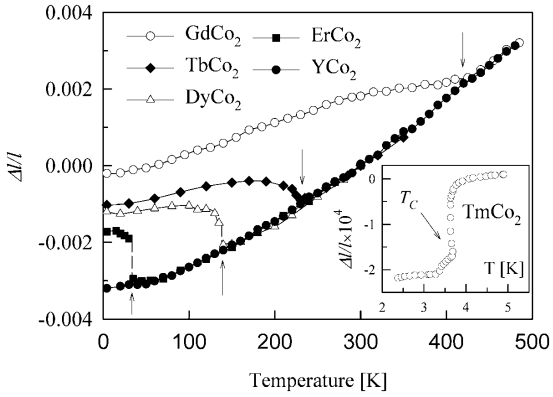

Figure 3.6. The linear thermal expansion of some $RECo_2$ compounds normalized to 300 K. (Figure from [21].)

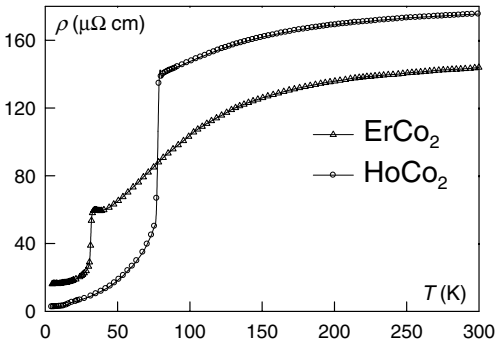

Figure 3.8. Temperature dependency of electrical resistivity for two $RECo_2$ compounds. (Figure from [52].)

In magnetic $RECo_2$ compounds the molecular field H_{m} exceeds the critical field H_c necessary to induce a ferromagnetic order in the d–electron subsystem. Owing to the negative sign of the f–d interaction, compounds with light RE elements are ferromagnetic (i.e., the sublattices are aligned parallelly), whereas those with heavy RE (Gd upon to Er) are accordingly ferrimagnetic. The properties of these compounds (especially in their paramagnetic state) cannot be satisfactorily explained while ignoring dynamic effects, such as spin fluctuations

(SF). The influence of SF on the physical properties can be seen most clearly in dynamic measurements, such as the transport phenomena.

Most of the magnetic and transport properties of the $RECo_2$ compounds are substantially influenced by the onset of the long–range magnetic order in the d–electron subsystem. The first–order magnetic phase transition in $DyCo_2$, $HoCo_2$ and $ErCo_2$ is accompanied by pronounced anomalies of the magnetization, the thermal expansion (see fig. 3.6, 3.7) and the transport properties (see fig. 3.8) at the Curie temperature. The large magnetovolume effect at T_C observed in $RECo_2$ compounds also originates from the onset of long–range magnetic order in the itinerant d–electron subsystem, while the anisotropic magnetostriction is mainly determined by the crystal–field interaction of the localized 4f–electrons with the magnetic RE ions.

Chapter 4

Experimental techniques

4.1 Sample preparation and characterization

Polycrystalline samples of $Er(Co_{0.97}X_{0.03})_2$ were prepared by an arc–melting of stoichiometric amounts of elements of at least 99.9% purity under an Ar atmosphere. In order to obtain good stoichiometric samples, the mass was fixed to $2.5 - 3\,g$ and during the melting procedure the samples were four times turned over. The samples were than wrapped up in a tantalum foil and sealed in a quartz tube under high vacuum ($10^{-6} - 10^{-7}$ mbar) and annealed at 950 °C for 50 hours in order to achieve good homogeneity.

Due to the high evaporation rate of some p–elements (Pb, As, Bi, Sb, In, see figure A.2 on page 44) in comparison to Co these samples were prepared as over stoichiometric in the p–element.

Analysis of x-ray diffraction pattern

Samples have been analyzed (as a fine powder) by x-ray powder diffraction at room temperature with a Seifert diffractometer (installed at the Department of Electronic Structures at the Charles University) working in the parallel beam geometry with Cu-K_α radiation ($\lambda = 1.54\,Å$) and graphite monochromator ($\cos\Theta_M = 0.89$) for suppression of incoherent diffraction.

The obtained results were analyzed by the `FullProf.2k` program [61] with the help of its graphical interface `WinPLOTR` [62].

4.2 Electrical–resistivity measurements

The temperature dependence of the electrical resistivity was measured by the standard four–point AC method (80 Hz) on bar–shaped samples with a cross section of typically $1 - 2\,mm^2$. The distance between the voltage contacts varied between $5 - 10\,mm$. Contacts were made by silver paint.

The contacted sample was glued on a non–conducting base to avoid short circuit through copper "cold finger". This can cause a difference in temperatures between

sample and "cold finger" where a Si diode for measuring temperature is placed. To suppress this effect, slow cooling and heating rates were chosen.

A constant current of typically 10 mA goes through a standard resistor (100 Ω) in series with a measured sample. Voltage between inner contacts of sample is measured by the lock–in amplifier SR830 DSP made by Stanford research systems (see figure 4.1). Measurements were performed in the temperature range 15 − 300 K using the closed–cycle refrigenerator controlled by temperature controller Leybold LTC60.

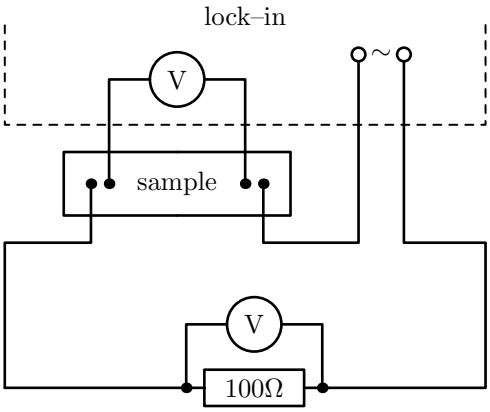

Figure 4.1. Wiring diagram of resistivity measurement.

The absolute error of resistivity measurements is mainly affected by the uncertainty of the geometrical factors and the occasional microcracks in the sample and is estimated to about 10%.

The magnetoresistivity (in fields up to 5 T) and some resistivity (in 0 T) measurements were performed[1] in the Joint Laboratory for Magnetic Studies (JLMS) using Physical Property Measurement System (PPMS) [65] (Quantum Design).

4.3 Magnetic measurements

All polycrystalline samples for bulk magnetic and susceptibility measurements were made of randomly oriented powder, fixed by a nonmagnetic glue in a small ampule. The mass of the powder sample was approximately 30 − 50 mg.

Magnetic properties were measured using SQUID magnetometr [64] (Quantum Design) installed at the Institute of Physics of Czech Academy of Sciences, which can achieve sensitivity of about 10^{-11} Am^2 in the magnetic moment determination. The magnetic moment of the sample is measured by the induction technique, which is most common in modern instruments.

The principle of this method is the measuring of induced voltage while moving the sample through the pickup coils. The induced voltage is given as

$$U = \frac{n\mathrm{d}B}{\mathrm{d}t} = nA\frac{\mathrm{d}B}{\mathrm{d}t} \tag{4.1}$$

where n is number of screws in coil and A in a cross section of the coil. The magnetic field is given as a sum of magnetization and magnetic intensity $B = \mu_0(M + H)$. Thus the change of the magnetic field caused by the extraction of sample out of the coil is $\Delta B = \mu_0 H$ and (4.1) can be written as

$$\int U\mathrm{d}t = nA\mu_0 M \ .$$

[1] with respect to application note [66]

With the help of this equation we are able to measure and calculate the magnetization M or the susceptibility $\chi = \partial M/\partial H$.

Induction measurements are performed by moving the sample relative to a set of pickup coils, either by vibration or one-shot extraction. In conventional inductive magnetometers, the voltage which is measured is induced by moving the sample with magnetic moment in a set of copper pickup coils. A much more sensitive technique uses a set of superconducting pickup coils and a SQUID to measure the current induced in superconducting pickup coils, yielding high sensitivity that is independent of sample speed during extraction.

In this experiment, the temperature was changed in the range $5 - 300\,\mathrm{K}$ (AC, DC susceptibility) with fields up to $5\,\mathrm{T}$ (magnetization curves).

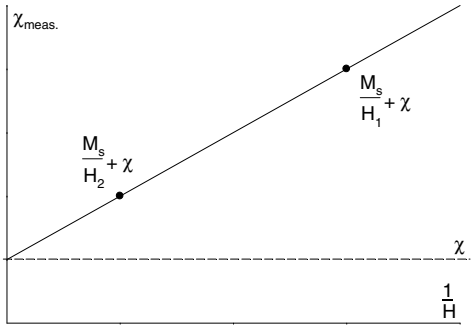

Figure 4.2. Extrapolation of $\frac{1}{H}$ to zero.

In the case of measurement of hi–temperature magnetization the experiment have been carried in two fields[2] H_1, H_2 to have a possibility to subtract the contribution of ferromagnetic phase impurity (the most common impurity in $ErCo_2$ compound is $ErCo_3$ with $T_c = 401\,\mathrm{K}$ [22]). The samples magnetization in the presence of impurity and external field is given as

$$M_i = M_s + \chi H_i \ , \quad i = 1, 2$$

where M_s is the saturated magnetization of impurity and χ is the susceptibility of $ErCo_2$. As a solution of this equations we obtain a susceptibility

$$\chi = \frac{M_1 - M_2}{H_1 - H_2}$$

which is in fact extrapolation of measured susceptibility to infinity — see figure 4.2.

4.4 Thermal expansion measurements

Micro–strain gages

The thermal expansion was measured using the micro–strain gages. The extension (contraction) of the strain gage and sample caused by the temperature change can be observed as resistivity change ΔR of the strain gage which depends on the change of sensor's length as well as on it's material. The relative change of resistivity is proportional to the temperature change [59]

$$\frac{R(T) - R(T = T_{\mathrm{ref}})}{R(T = T_{\mathrm{ref}})} = \left(\frac{\Delta R}{R}\right)_{\mathrm{measured}} = (\beta_g + (\alpha_s - \alpha_g)\, g)\, \Delta T \ , \qquad (4.2)$$

[2] high enough for saturation of magnetic impurity

where β_g is the thermal coefficient of grid resistance, $\alpha_{s,\,g}$ are thermal expansion coefficients of sample and grid and g is gage factor of the strain gage.

If $\frac{\Delta R}{R}$ is measured, the thermal expansion of the strain gage can be derived from (4.2). In order to measure the thermal expansion of the sample, the strain gage is fixed on it's surface by a special glue. The measured thermal expansion then contain contributions from the sample (temperature dependence of the length) and strain gage (temperature dependence of the length and conductivity). We have to measure a reference sample (in this case TiSi with negligible thermal expansion for Micro–Measurements strain gages and copper[3] for Kyowa strain gages) to obtain the temperature dependence $\frac{\Delta R}{R}$ of a strain gage. Equation (4.2) can be rewritten into the form where effects of grid and sample are separated as follows:

$$\left(\frac{\Delta R}{R}\right)_{\text{measured}} = (\beta_g + \alpha_g g) + \alpha_s g \Delta T = \left(\frac{\Delta R}{R}\right)_{\text{SG contribution}} + g\left(\frac{\Delta L}{L}\right)_{\text{sample}}$$

$$\left(\frac{\Delta L}{L}\right)_{\text{sample}} = \frac{1}{g}\left(\left(\frac{\Delta R}{R}\right)_{\text{measured}} - \left(\frac{\Delta R}{R}\right)_{\text{SG contribution}}\right) .$$

The strain–gages contribution can be calculated from measurement of sample with known thermal expansion (Cu/TiSi)

$$\left(\frac{\Delta R}{R}\right)_{\text{SG contribution}} = \left(\frac{\Delta R}{R}\right)_{\text{measured on Cu/TiSi}} - g\left(\frac{\Delta L}{L}\right)_{\text{Cu/TiSi}} .$$

The used strain gages have the following characteristics (SK-350 type from Micro-Measurements and SKF-5414 type from Kyowa)

	Micro–Measurements	Kyowa
gage factor g	2.04 ± 0.02	1.88 ± 0.03
resistance of strain gage R (Ω)	350.0 ± 1.4	120.0 ± 0.8
temperature coefficient of g ($10^{-2}\,\%\,\mathrm{K}^{-1}$)	-1.4 ± 0.2	-1.65 ± 0.18

Temperature dependences of strain gages resistivity were measured in JLMS using PPMS.

Temperature dependent X-ray measurement

Temperature dependences of lattice parameter were measured by x-ray powder diffraction with a Siemens (D-500) diffractometer working in the Bragg-Bretano geometry with Co-K_α radiation ($\lambda = 1.78\,\text{Å}$). The system is equipped with a helium–gas–flow cryostat (Oxford Instruments CF1108T). Liquid helium and nitrogen were used as a cooling medium.

The sample was placed on a silicon single–crystalline plate. The Si plate is cut in $\langle 111 \rangle$ direction in order to divert the strong reflection. The application of an additional sample holder is necessary because of a polycrystalline nature of a "cold finger". However, this interface can cause a strong temperature gradient.

[3] thermal–expansion given in [35]

Chapter 5

Results

5.1 Sample preparation and characterization

Ten samples of nominal composition $ErCo_{1.94}X_{0.06}$ (for X = Al, Si, Ga, Ge, As, In, Sn, Sb, Pb, Bi) were prepared and checked for a phase composition in x–ray and microprobe experiments. Samples with X = Al, Si, Ga, Ge, In have a significant amount of substituent in the base phase $ErCo_2$ and not only in foreign phases and shows a shift in transition temperature (compared to $ErCo_2$). A structural and phase characteristic is given in table 5.1.

X	r_X(Å)	a (Å)	% X in Co	foreign phases
Al	1.43	7.1640(5)	———	———
Si	1.176	7.1588(2)	2.7	$\sim 6\%$ $ErCo_3$
Ga	1.22	7.1678(4)	3.2	$\sim 7\%$ $ErCo_3$, $\sim 1\%$ Er
Ge	1.225	7.1670(4)	2.7	———
In	1.62	7.1511(3)	2.0	trace amount of $ErCo_{0.92}In_{0.06}$ phase

Table 5.1. Table of metallic radii r_X (of pure X metal) [11], lattice parameter a of $Er(Co_{0.97}X_{0.03})_2$ (determined from the x–ray diffraction experiment), amount of the X substituent in cobalt (microprobe analysis) and information of foreign phases in sample (microprobe and x–ray experiments).

Typical one phase and multi–phase x–ray powder diffraction data are given in figures 5.1 and A.3. Theoretically the amount of substituent can be determined from these powder diffraction patterns. As can be seen in figure A.4, the difference in patterns is bigger than a uncertainty of measurement (which is proportional to $\sqrt{N}$), but it is not still enough to get a stable solution of Rietveld refinement (because of correlation between occupancy and Debye–Waller factor). The diffraction pattern calculated for In substitution was taken as an example, because In is the best candidate due to its position[1] in periodic table of elements (as compared with Er and Co).

[1] If we want to see difference in diffraction pattern of substituted and notsubstituted samples we need to have big difference in atomic formfactors, which corresponds to a different number of electrons.

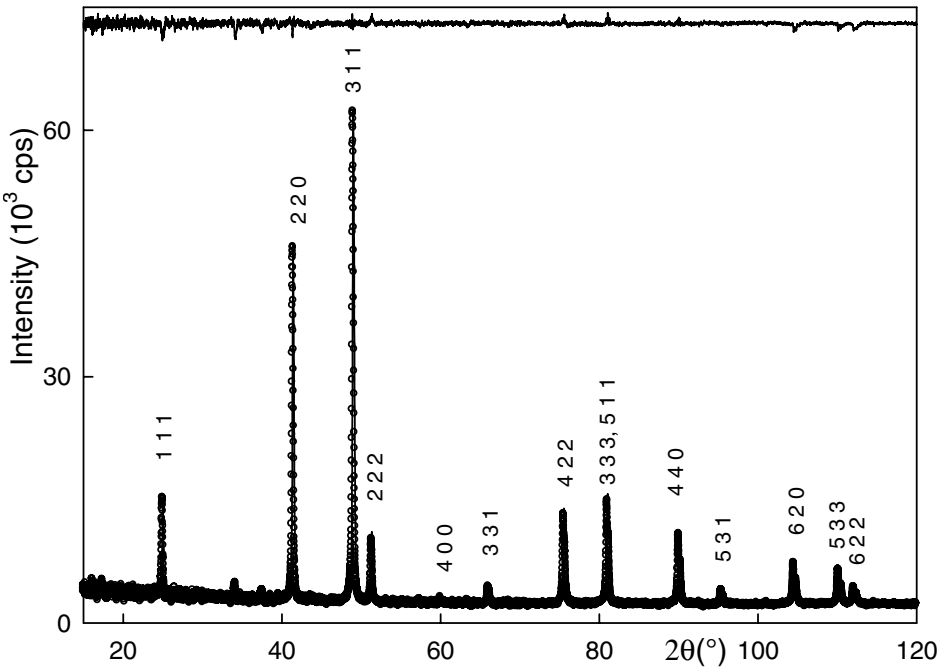

Figure 5.1. Example of one phase ($ErCo_{1.94}In_{0.06}$) powder diffraction pattern.

5.2 Transport properties

Electrical resistivity

Figure A.5 depicts the temperature dependence of resistivity normalized to the resistivity at room temperature. The saturation behavior and approach to linearity is observed for all samples at high temperatures. Figure 5.2 shows the temperature dependence of the electrical resistivity of studied compounds in the vicinity of transition temperatures. In figure A.6 is plotted a first derivative[2] of resistivity with respect to temperature.

X	T_c (K)	ϱ_{spd}	ϱ_0
Al	43.2	5.6	6.5
Si	43.8	3.4	7.8
Ga	43.5	4.6	6.3
Ge	47.3	4.0	9.8
In	52	4.8	5.3

Table 5.2. Critical temperature T_c, spin–disorder resistivity ϱ_{spd} and resistivity ϱ_0 extrapolated to 0 K in units ($10^{-7}\Omega\,m$)

The transition is characterized by a discontinuity ϱ_{spd} (which corresponds to the maximum in the first derivation) at the ordering temperature. The phase transitions are of the first–order (sharp maxima in first derivation) in the case of Ga, Al and Si, and changes to the second–order (Ge and In) with increasing temperature at which the transition is realized.

Table 5.2 summarises basic data obtained from the resistivity measurement. The transition temperature T_C was obtained as the temperature of the maximum in the first derivation.

[2]obtained from quadratic interpolation of measured data

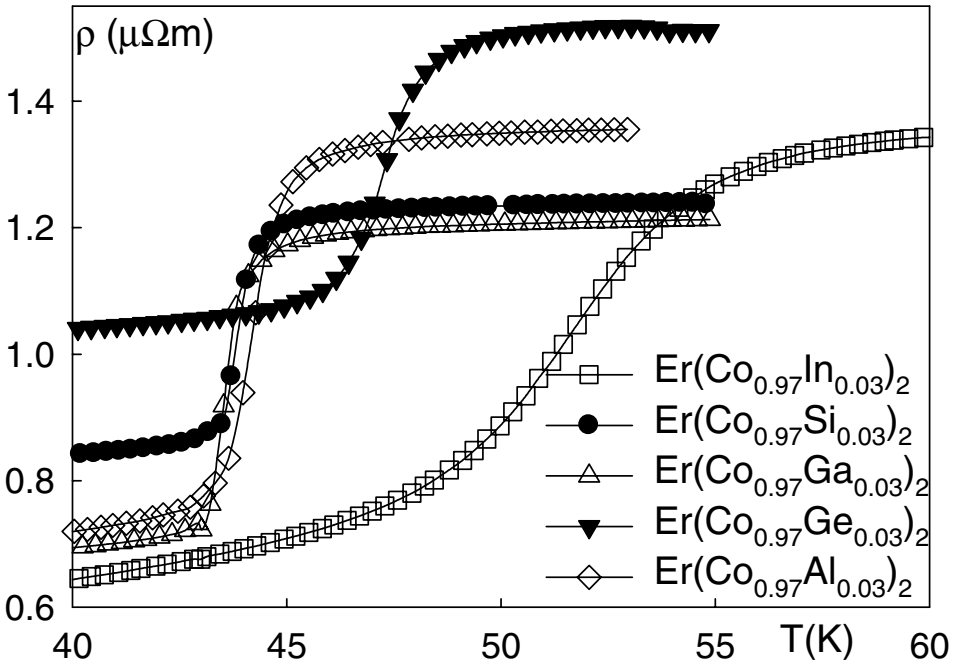

Figure 5.2. Resistivity as a function of temperature in the vicinity of critical temperature.

5.3 Magnetic properties

Magnetization

The temperature dependencies of the magnetization measured in a field 0.01 T is presented in figure 5.3. The different character of magnetic phase transitions is verified: for samples substituted with Si, Al and Ga, a discontinuous change of the magnetization occurs at T_c, while for other samples a change of magnetization around T_c is gradual and broadened. The critical temperatures obtained from this plot and from the AC–susceptibility measurement are summarized in table 5.3.

The measured high temperature dependencies of magnetization was extrapolated to an infinity field, as described in chapter 2. For the suppression of the phase transition effects, extrapolated data from $T \approx 200\,\mathrm{K}$ were only taken for fitting the equation (2.9)

$$\chi = \frac{C'}{T - \Theta'_p} + \chi_{ee} \ .$$

The temperature of the phase transition determined from the heat capacity measurement was used as Θ'_p — see fig. 5.3. This was done to obtain better stability of the nonlinear fit — fixing one of the variables ensures that we obtain only one solution with significant minimum. The data obtained from the fit are in table 5.3.

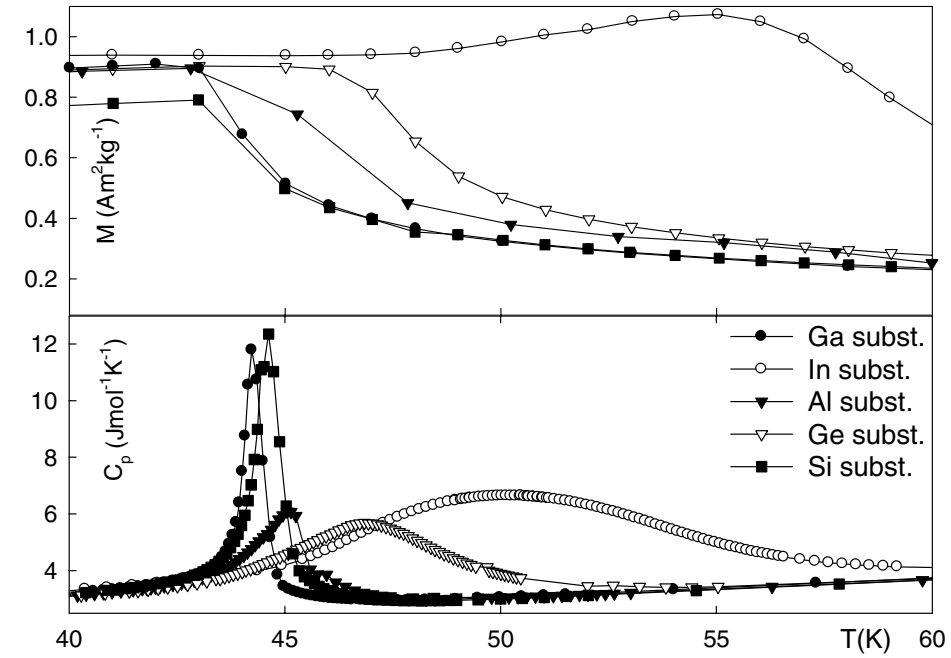

Figure 5.3. Magnetization curves (see fig. A.1) and specific heat in the vicinity of the transition temperature.

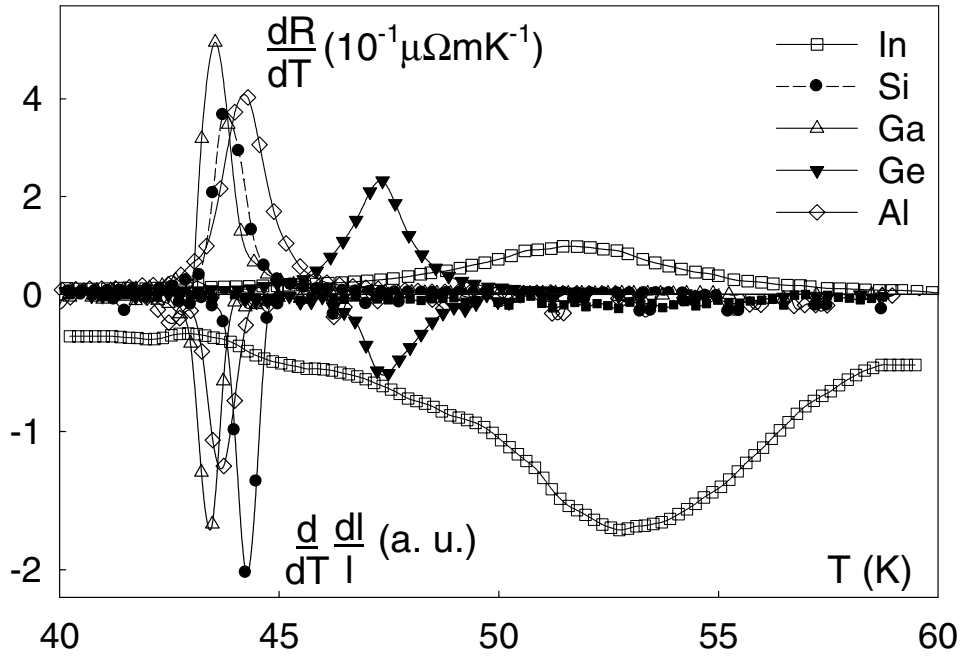

Figure 5.4. Comparison of derivatives of the thermal expansion (smoothed and multiplied by 20 for the In case) and the resistivity. See figures A.6 and A.23.

X	Al	Si	Ga	Ge	In
T_c (K)	44.5	44.5	44	47	56
Θ' (K)	45.2	44.6	43.7	46.8	50
C'	1.114	1.028	1.052	0.987	1.052
χ_{ee}	6.61 ± 0.13	8.89 ± 0.12	7.72 ± 0.14	8.753 ± 0.11	6.93 ± 0.14

Table 5.3. Critical temperature T_c from magnetization and heat capacity measurements and parameter of fit to (2.9) — C' in $10^{-4}\,\mathrm{Km^3mol^{-1}}$ and χ_{ee} in $10^{-8}\,\mathrm{m^3mol^{-1}}$. The error is for C' $3 \times 10^{-7}\,\mathrm{Km^3mol^{-1}}$.

Magnetization izotherm and Arrott plot

Figures A.13—A.15 show measured magnetization isotherms. Clear metamagnetic transitions was observed in compounds with substitution of Al, Si and Ga, whereas in indium substituted sample metamagnetic transition did not occur (Arrott plot (fig. A.18 shows monotonic behavior). From the Arrott plot we see that the germanium substituted sample (fig. A.17) seems to be on the edge of observability of metamagnetismus.

The critical field B_c has the same behavior as in the magnetoresistivity measurements – increases with the increasing temperature (for comparison see 5.7) whereas step of magnetization ΔM at metamagnetic transition is decreasing and vanishes in higher temperatures ($T_c+ \approx 10\,\mathrm{K}$).

Magnetocaloric phenomena

Isothermal entropy change (see fig. 5.5) can be calculated from the magnetization isotherms using one of Maxwell's relations [39]

$$\left(\frac{\partial M}{\partial T}\right)_H = \left(\frac{\partial S}{\partial H}\right)_T$$

in the form

$$-\Delta S_m = S_H - S_{H=0} = \int \left(\frac{\partial M}{\partial T}\right)_H \mathrm{d}H \ . \tag{5.1}$$

Under the assumption that the susceptibility has the MCW behavior (2.9)

$$\chi = \frac{C'}{T - \Theta'_p} + \chi_{ee}$$

the entropy change should have the temperature dependence

$$-\Delta S_m \sim \left(T - \Theta'_p\right)^{-2} \ .$$

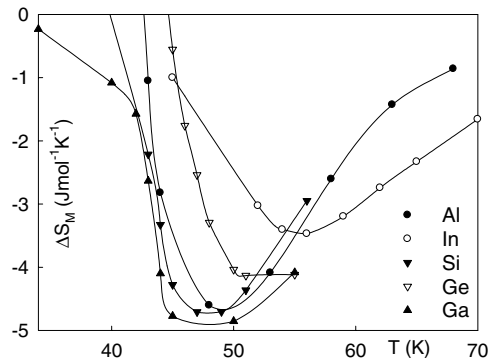

Figure 5.5. Calculated isothermal magnetic entropy change in magnetic fields up to 5 T.

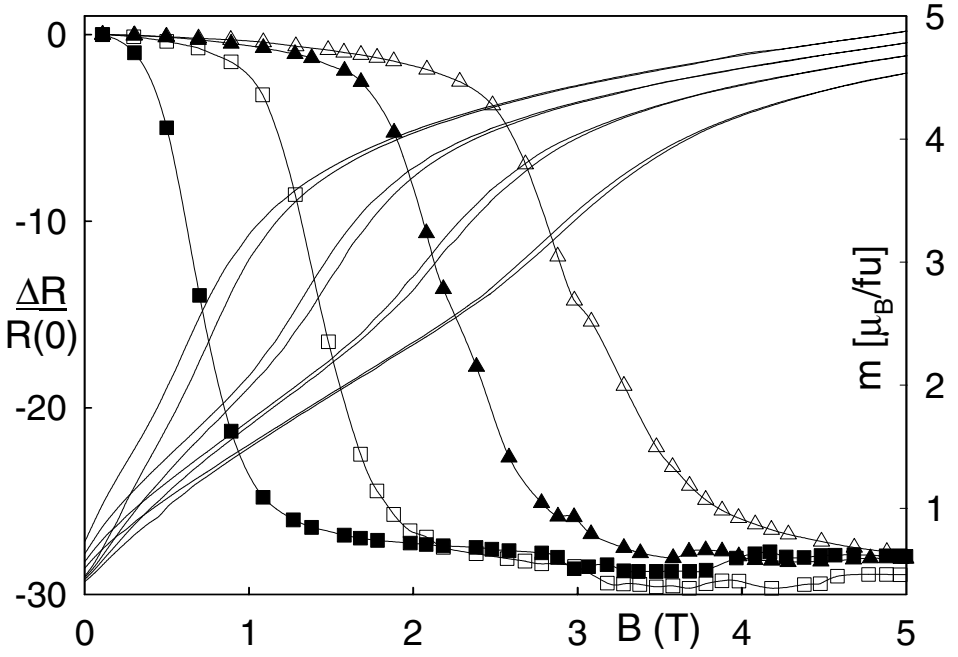

Figure 5.6. Field dependence of the magnetization and magnetoresistivity of $ErCo_{1.94}Si_{0.06}$ at the same temperatures T = 45, 47, 49, 51 K (see figures 5.7, A.7, A.13).

as deduced from (5.1).

The calculated isothermal magnetic entropy change have the same temperature evolution as that in $ErCo_2$ and is achieving a half of its value [42]. This can be caused by numerical errors (the measurement of isothermal magnetization wasn't done for this purposes and is not quite enough detailed in temperature axes). The magnetocaloric phenomena should be investigated in more detail within measurements of the specific heat in magnetic fields.

Magnetoresistance

The results of the transversal magnetoresistivity measurements are presented in figures A.7, A.8 and A.9. Drops of resistivity above T_C in all compounds, except In substituted sample, are observed from 25% (in the case Ge substitution) to 40% (in the case Al substitution). This effect is related to the metamagnetic transition from the paramagnetic to the ferrimagnetic state (as can be seen from the magnetization measurement). The critical field B_c increases with temperature (see fig. 5.7) whereas the resistivity step stays approximately the same. In the indium substituted sample a continuous and gradual decrease of magnetoresistivity against the field was observed.

The evolution of phase transitions in fields can be seen in figures A.10 – A.12. The evolution is the same as in the case of $ErCo_2$ — the drop becomes broader and is shifted to higher temperatures.

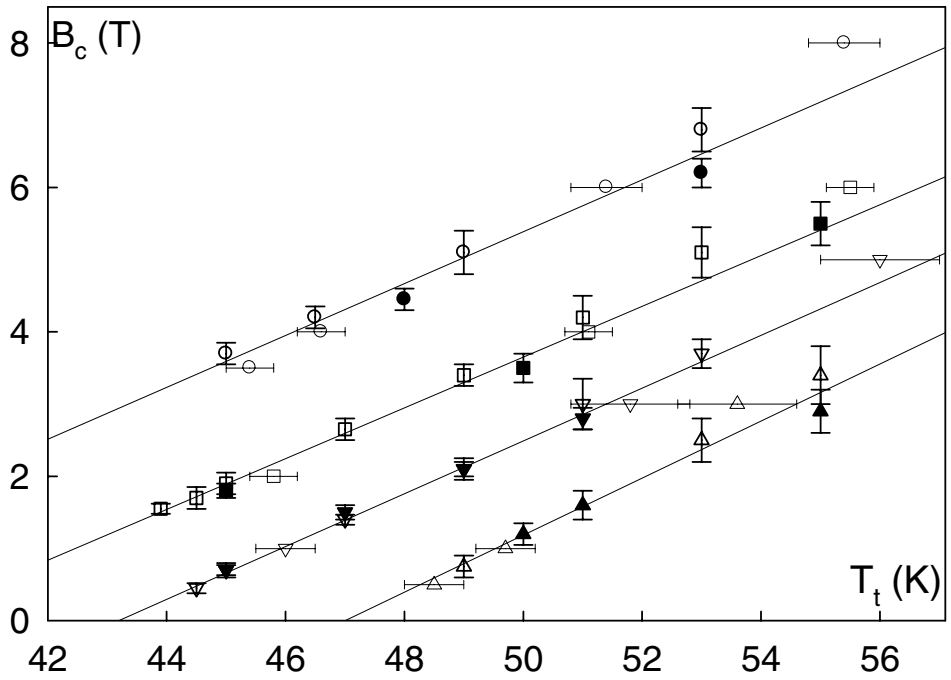

Figure 5.7. Temperature dependence of critical field for metamagnetic transition. • — Al substitution, ■ — Ga subst., ▲ — Ge subst., ▼ — Si subst. The data from Al (Ga) subst. sample are for clarity shifted by 2.5 (resp. 1) T higher.

In figure 5.7 the linear dependence between the transition temperature and critical field can be seen. The open marks are the data determined from the magnetoresistance experiment whereas the solid marks represents the data from the magnetization isotherms. For comparison, data obtained from the measurement at constant field during heating are presented (points with horizontal error bars). As can be seen, the data from magnetization and magnetoresistivity measurements in increasing field are in very good agreement. The lines represent weighted linear fits of results.

The observed linearity cannot be explained either directly from the theory, or from the results measured on nonmagnetic analogues $Lu(Co_{1-x}Ga_x)_2$ [40], which predicts and follows a shifted T^2 law in low temperatures. The reason can be, that for small arguments the T and T^2 curves are not very different, whereas the high field plot could be more curved (as it is in the case of pure $ErCo_2$ [15]). As a confirmation of this idea, the behavior in higher fields ($4-5\,\mathrm{T}$), where the data are just above the fit, can be taken.

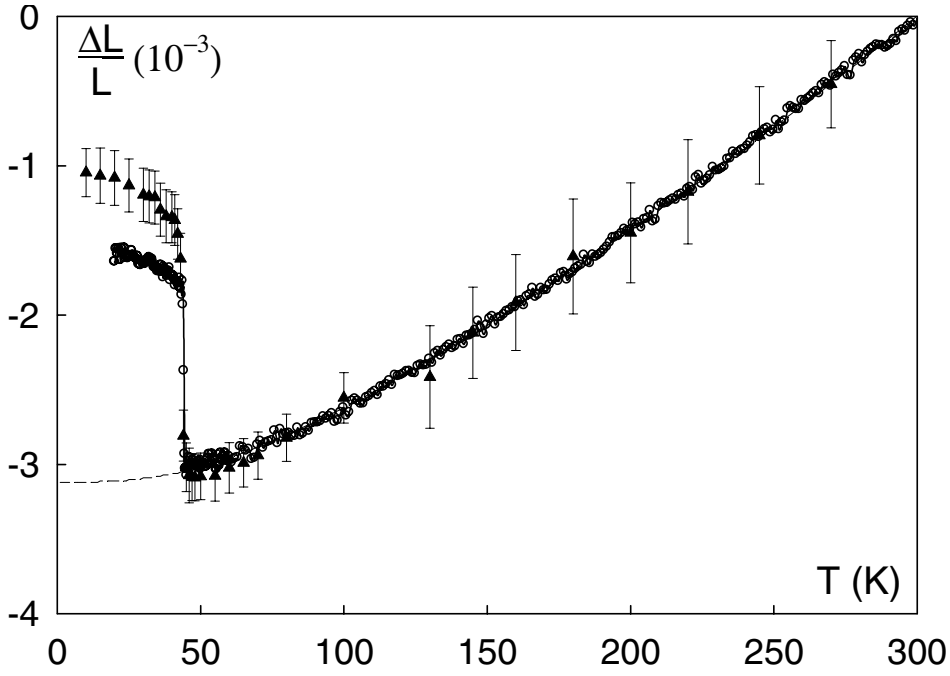

Figure 5.8. Temperature dependence of the thermal expansion of $ErCo_{1.94}Si_{0.06}$.

5.4 Magnetovolume effects

The thermal expansion curves of $ErCo_{1.94}X_{0.06}$ compounds are in figures 5.8 and A.19 – A.21. Above T_C, the thermal expansion of all the samples indicate the paramagnetic behavior. The abrupt lattice expansion observed at T_C is attributed to the positive magnetovolume effect, accompanying sudden formation of the Co magnetic moment. The relative volume change in the cubic structure is determined by the expression $\omega_s = 3\Delta L/L$ where $\Delta L/L$ is the linear thermal expansion.

X	Al	Si	Ga	Ge	In
T_c (K)	43.7	44.2	43.5	47.5	53
ω_s (10^{-3})	4.20	4.46	4.28	4.03	3.31
$K_1 + K_1'$	2.6 ± 1.2	9.7 ± 1.0	8.2 ± 1.0	9.8 ± 1.0	9.8 ± 0.8
K_2	1.35 ± 0.06	1.03 ± 0.05	1.05 ± 0.05	0.91 ± 0.04	0.95 ± 0.04

Table 5.4. Critical temperature T_c from the thermal expansion measurements. Parameters of fit ($K_1 + K_1'$ in $10^{-9}\,K^{-2}$ and K_2 in $10^{-5}\,K^{-1}$) to theoretical expression (2.22) were calculated for fixed Debye temperature, determined from heat capacity measurement as (240 ± 10) K.

Values of the relative volume change and parameters of the theoretical fit (2.22) are summarized in table 5.4. The parameters $K_1 + K_1'$ and K_2 are in fact the same (except Al subst.) as for YCo_2 [21]. We may conclude that the substitution does not influence the behavior of the thermal expansion in the paramagnetic range, i.e. the thermal expansion can be described as a sum of electronic and phononic part with

spin–fluctuation enhancement (magnetoelastic part).

The sample with Al substitution shows only one third of the value $K_1 + K_1'$ as compared to other substitutions. This can have two reasons — physical and experimental. The physical one would be, that the Al substitution would cause a suppression of spin fluctuations in the paramagnetic state or a dramatic change of Debye temperature. If we consider, that for non-SF system is the value of $K_1 + K_1'$ typically $4 \times 10^{-9}\,\mathrm{K}^{-2}$ [21], we can eliminate this cause. The change of the Debye temperature is out of question in these small substitutions, so we may conclude, that this "noise" comes from imperfect gluing or from hidden cracks in sample.

For comparison, the temperature dependencies calculated from x–ray diffraction data are depicted in the same figures. These data are critically dependent on the accuracy of determination of lattice parameters at room temperature — they are calculated from relationship

$$\frac{\Delta L}{L} = \frac{L(T) - L_{300\,\mathrm{K}}}{L_{300\,\mathrm{K}}} = \frac{a(T) - a_{300\,\mathrm{K}}}{a_{300\,\mathrm{K}}}$$

and the error manifest itself as a shift in $\frac{\Delta L}{L}$ axes.

Another discrepancy between x–ray and dilatometric measurements is in position of the critical temperature, which is shifted to lower temperatures in the case of x–ray measurements. The reason is that a temperature difference can be between the sample and thermometer (see page 29).

Nevertheless, the agreement between the x–ray and dilatometric studies is very good as compared with the difference of these methods — x–ray measurement is in fact *in situ* measurement whereas dilatometric study is a typical bulk method. It should be noted, that the use of strain–gages brings problems as the uncertainty in the quality of glueing or the possibility of microcracks under the surface, which can be partly detected in high–pressure measurement. There is also a principal problem, originating from the expectation, that the strain–gages on the reference sample and the analyzed sample is identical, which can be fulfilled only to some extent.

Data from dilatometric measurement are summarized in figures A.22 and A.23. The transition temperatures agree well with the other measurements see fig. 5.4.

Rhombohedral distortion analysis

Besides the volume expansion, a rhombohedral distortion of the cubic lattice along the <111> easy magnetization direction was observed below T_C. The parameters of the rhombohedral distortion were calculated from the splitting of the diffraction line 620 (cubic structure notation) below T_C into the 620 and $\bar{6}20$ lines (rhombohedral structure notation).
For a small rhombohedral distortion ε

$$\alpha_\mathrm{R} = \frac{\pi}{2} - \varepsilon$$

the interplanar spacing of hkl crystallographic planes is approximated by [44]

$$d_{hkl}^2 = \frac{a_\mathrm{R}^2}{h^2 + k^2 + l^2 - 2\varepsilon(hk + kl + hl)}\ .$$

For selected lines we have obtained

$$d_{620}^2 = \frac{a_{\mathrm{R}}^2}{40 - 24\varepsilon}$$
$$d_{\bar{6}20}^2 = \frac{a_{\mathrm{R}}^2}{40 + 24\varepsilon}$$

and the rhombohedral lattice parameters a_{R}, α_{R} can be calculated by solving this system of equations.

X	a_{R} (Å)	α_{R} (°)	$-\lambda_{111}(10^{-3})$
Si	7.1505	90.12	2.17
Ga	7.1572	90.10	1.80
In	7.1458	90.11	1.84

Table 5.5. Parameters of the rhombohedral distortion.

The line splitting was examined by the profile analysis in the program `DIFPATAN` [63]. The line (measured at 10 K) was approximated by the Pearson VII function. The profile parameters were mutually bound[3] and only the line position was taken as independent for these two lines. Before the profile analysis the data were shifted in order to correct the zero position of the position sensitive detector. The zero–shift was obtained from the Rietveld refinement of the entire diffraction pattern. The obtained values are summarized in table 5.5.

The results are in very good agreement with the previous work [13] (where the profile fitting was done in a different way) as can be seen from figure 5.9.

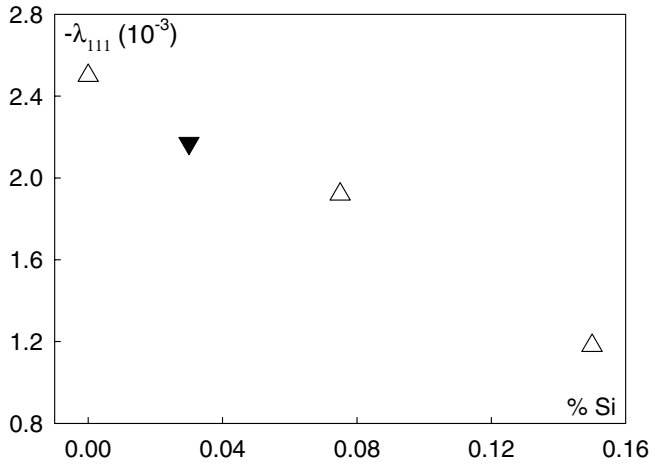

Figure 5.9. The evolution of magnetostrictive coefficient λ_{111} with substitution of Si. (Open marks are the data taken from [13].)

[3] In this case the splitted lines should be identical and only shifted (and for this reason it is impossible (in polycrystalline sample and this line) to determined the sign of ε).

Chapter 6

General discussion

The induced Co moment and the 4f–3d interaction

The magnetic ordering in heavy $RECo_2$ compounds is mainly determined by the 4f–3d exchange interaction. The volume change with the onset of magnetic ordering mainly reflects the d band polarization which causes an induced Co magnetic moment. Therefore, the magnetovolume effect in magnetic compounds containing 3d elements is explained in the framework of an itinerant model. The relation of the magnetovolume effect ω_s and the magnetic moment μ_{Co} in the case of $RECo_2$ may be expressed by the following phenomenological expression

$$\omega_s \sim n(\Delta\mu_{Co})^2$$

where $\Delta\mu_{Co}$ is the Co magnetic moment gained below T_C.

Under the assumption that n is invariant for non–substituted and substituted samples (which was verified for $Er(Co_{1-x}Si_x)_2$ samples up to $x = 0.1$ [12]) we can calculate the induced Co moment $\Delta\mu_{Co}(X)$ of X–substituted sample as

$$\Delta\mu_{Co}(X) = \Delta\mu_{Co}(0)\sqrt{\frac{\omega_s(X)}{\omega_s(0)}}\ , \qquad (6.1)$$

where $\Delta\mu_{Co}(0) = 1.07\mu_B$ is the Co moment of $ErCo_2$ [38], $\omega_s(X)$ is the magnetovolume change corresponding to the doped sample and $\omega_s(0)$ to the not–doped sample. Values calculated from the data from table 5.4 are listed in table 6.1. The value obtained for the Si doped sample is in a good agreement with previous results, measured on $Er(Co_{1-x}Si_x)_2$ samples [12].

X	$\Delta\mu_{Co}$ (μ_B)	υ_{RE-Co}
Al	1.07	-1.83 ± 0.06
Si	1.11	-1.75 ± 0.04
Ga	1.09	-1.88 ± 0.05
Ge	1.06	-1.97 ± 0.04
In	0.95	-2.10 ± 0.06

Table 6.1. Values of induced Co moment and molecular field coefficients (in $10^6\,m^{-3}mol$). Errors are calculated from the errors from fitting experimental data.

In the same table values of υ_{RE-Co} are mentioned that have been calculated from (2.12) and (2.13) and data listed in table 5.3.

The values of υ_{RE-Co}, calculated using (2.12) and (2.13) and the data from the table 5.3 are also listed in the table 5.3. As can be seen, there is no significant effect which can be ascribed to the different substitutions.

Quenching of spin fluctuations

The ϱ_{mag} contribution in (2.16) consists of two contributions above T_{c}: first contribution comes from the scattering of conduction electrons on disordered 4f moments, second contribution is caused by the scattering of conduction electrons on spin fluctuations of 3d spins. First contribution plays a dominant role in compounds with nonmagnetic transition element as $RENi_2$ and $REAl_2$. In $RECo_2$ compounds, the resistivity is strongly influenced by the spin–fluctuation of the moment on Co–sites above T_{c}. From the study of the resistivity of YCo_2, YNi_2 and YAl_2 is known [21], that the enhancement in resistivity of YCo_2 is due to the scattering of the conduction electrons on Co–3d sites. By substituting Co by p–element, the resistivity behavior is modified, but the temperature dependence have the following common characters:

- Above T_{c}, the resistivity tends to the saturation at high temperatures (fig. A.5). This saturation behavior in the paramagnetic region is similar to the case of YCo_2, it is explained to be due to the suppression of the spin fluctuations on the Co–3d sites [28].
- Sharp discontinuities at T_{c} are observed in the resistivity corresponding to the first–order transition for all substitutions (except indium, where a second order phase transition was observed). The drop of resistivity is reduced in comparison to $ErCo_2$ [12].

The resistivity behavior of the heavy rare–earth $RECo_2$ compounds in the critical region around T_{c} is usually explained in the following scenario — the resistivity above T_{c} is mainly affected by a spin–disorder scattering on the paramagnetic rare–earth moments and by a electron spin fluctuation scattering depending on the dynamics of spin fluctuations in the Co–3d band. With decreasing temperature, the 4f moments which order ferromagnetically at T_{C} act via strong exchange interaction on the Co–3d states. When this action is sufficient to split the 3d majority and minority subbands, the spin fluctuations at the Co–sites are quenched and the 3d–band metamagnetic state is induced by the first order transition. Consequently, the scattering is drastically suppressed, which yields the the drop of resistivity.

The total magnetoresistance of itinerant magnetic compound is given as

$$\frac{\Delta\varrho}{\varrho}(T,H) = \left(\frac{\Delta\varrho}{\varrho}\right)_{\mathrm{c}}(T,H) + \left(\frac{\Delta\varrho}{\varrho}\right)_{\mathrm{sf}}(T,H)$$

where $\left(\frac{\Delta\varrho}{\varrho}\right)_{\mathrm{c}}(T,H)$ is the positive contribution due to the cyclotron motion of conduction electrons and $\left(\frac{\Delta\varrho}{\varrho}\right)_{\mathrm{c}}(T,H)$ is the negative contribution caused by the spin fluctuations. The huge negative drop in magnetoresistance was observed [12] for $ErCo_2$ (60%), caused by the quenching of the spin fluctuations above T_{c} at transition field B_{c}. The observed field value of MT in magnetization curve coincides with the value of the field where the sharp huge drop of resistivity takes place on an isothermal magnetoresistance curve and have the same evolution with the temperature — see figure 5.7. Therefore the large negative magnetoresistance step at B_{c} is ascribed to the first order phase transition from paramagnetic to ferrimagnetic state.

Chapter 7

Conclusions and outlook

In this work, experimental results of $ErCo_{1.94}X_{0.06}$ pseudobinary compounds with X=Al, Si, Ga, Ge, In are reported.

The results and their analysis have been mainly focused on the magnetic phase transitions and the magnetovolume effect and the induced Co moment. The first order magnetic phase transitions were observed in the case of Al, Si and Ga substitution, which changes to the second order in the case of Ge and In. The shift in transition ranges from 10 K (Al substitution) to 20 K (In substitution) compared to the not substituted sample. Clear metamagnetic transitions were observed in all compounds (except In subst.) on the magnetization and the magnetoresistance curves.

The magnetovolume effect in $ErCo_2$ can be increased (Si, Ga) or decreased (Ge, In) with the substitution of a p–element. The maximum change of induced Co moment, determined from magnetoelastic measurements, is about 10% in the case of Al and 20% in the case In substitution, respectively.

In order to understand the behavior of In substitution samples with different composition should be prepared to see the evolution within the substitution amount.

Moreover, the substitutions which cannot be prepared by direct melting (e. g. As) may be prepared using the natural solutions of these elements in the Co matrix (CoAs and Co_2As in the case As etc.).

The suggested study is the outline of my further work in the field of studying the evolutions of phenomena, concerning this type of materials.

Appendix A

Graphs

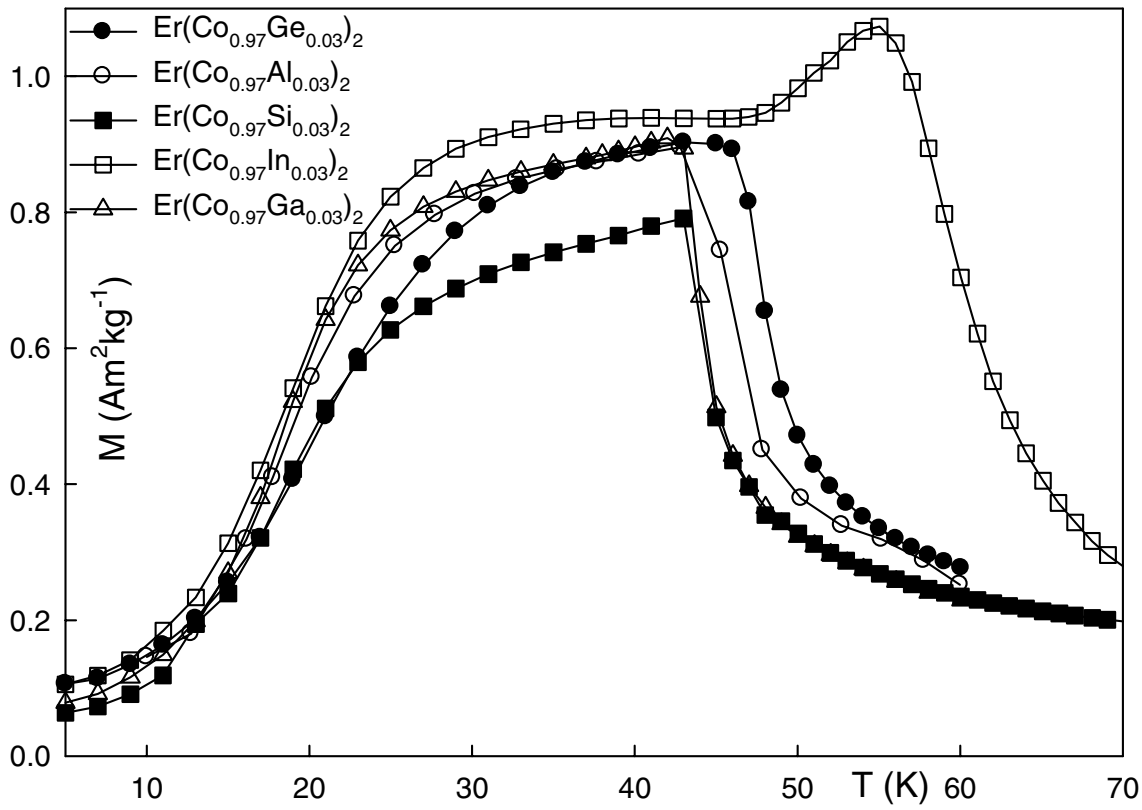

Figure A.1. Magnetization curves after ZFC in field 0.01 T.

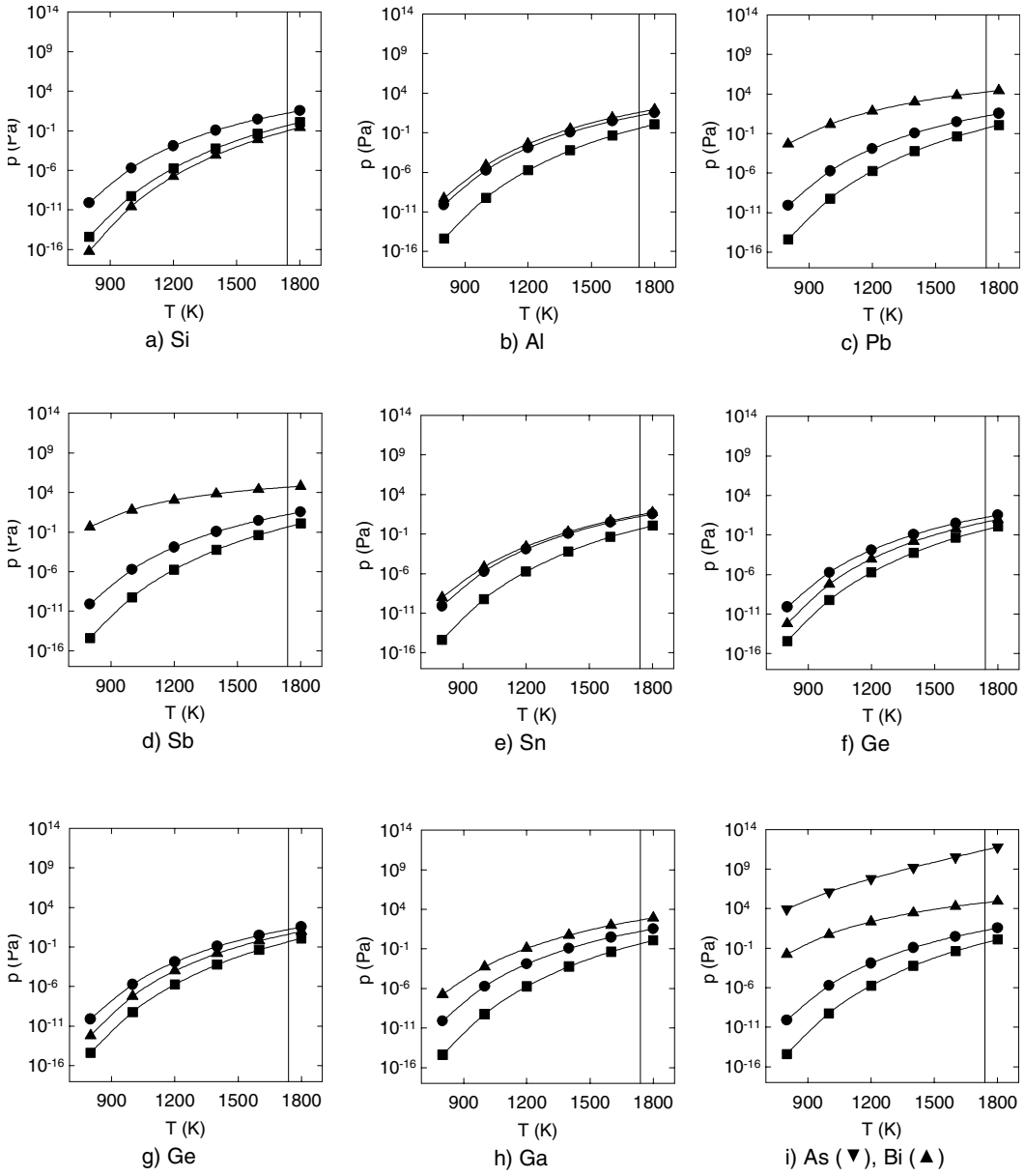

Figure A.2. Vapor pressure of Er (•), Co (■) and p–element (▲) [53]. Vertical lines represent melting point of erbium and cobalt (it's almost the same — 1768 K, 1770 K respectively [60]).

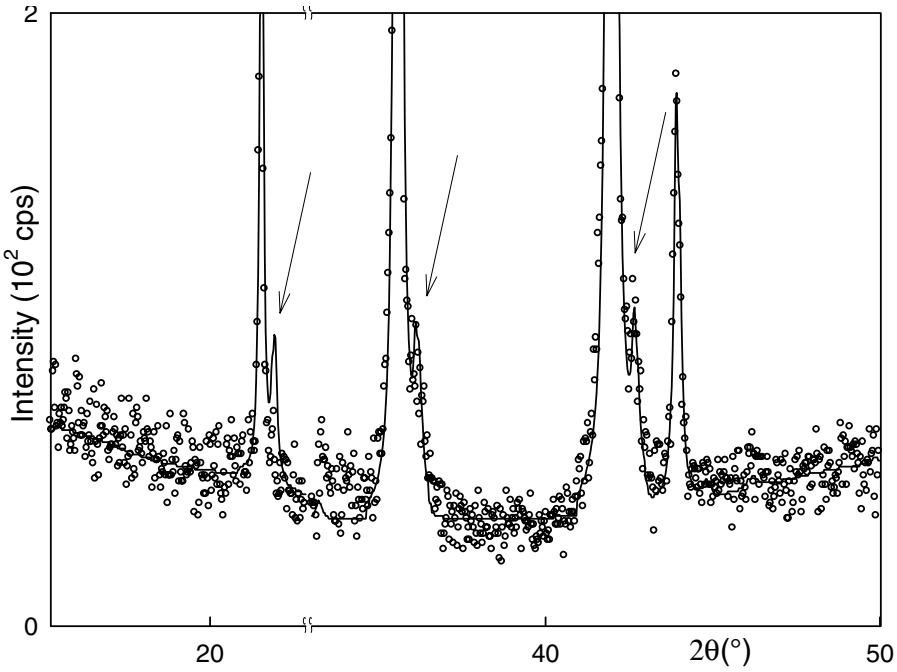

Figure A.3. Example of the two phases ($ErCo_{1.94}Si_{0.06}$) powder diffraction pattern. Arrows shows the reflections from the foreign phase ($ErCo_3$).

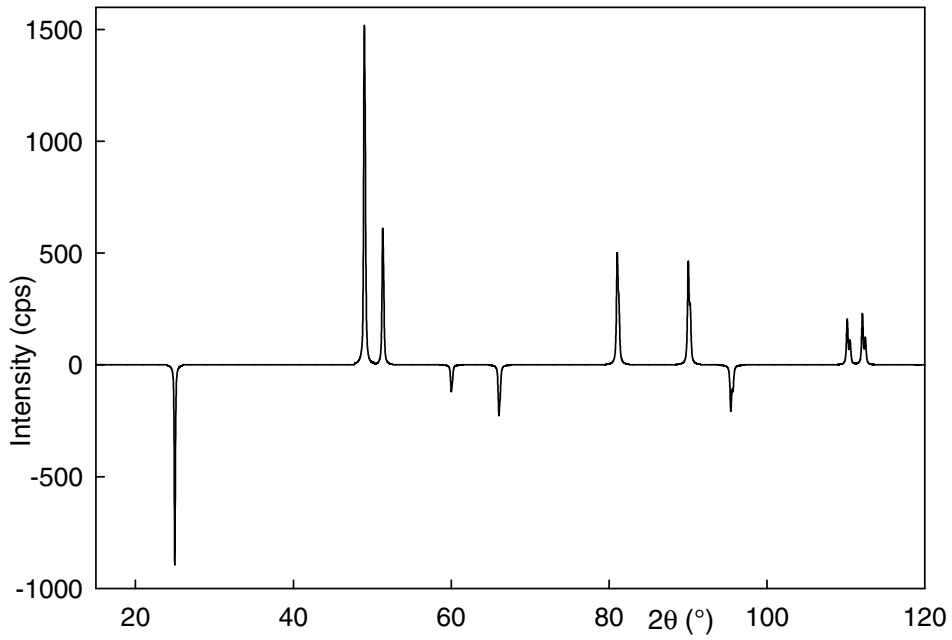

Figure A.4. Calculated difference of intensities in substituted and nonsubstituted sample (I($Er(Co_{0.97}In_{0.03})_2$) - I($ErCo_2$)). For number of counts see figure A.4.

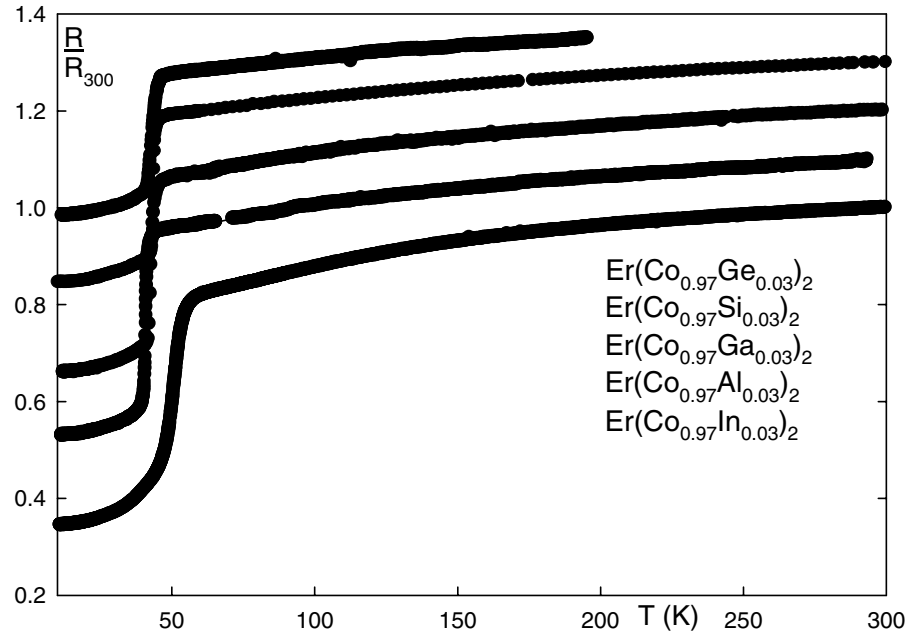

Figure A.5. Temperature dependences of resistivity normalized to the resistivity at room temperature.

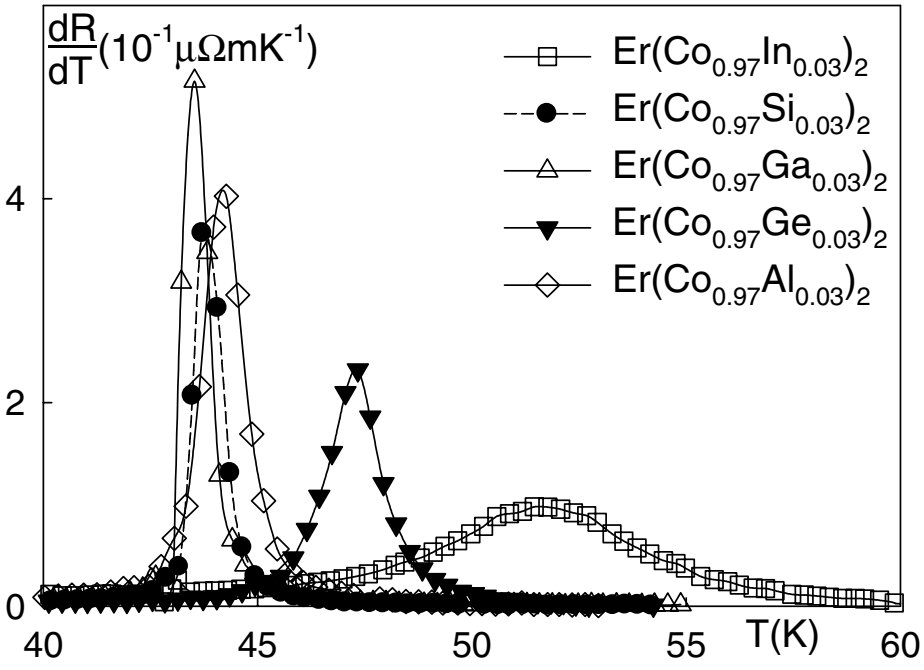

Figure A.6. Derivation of resistivity (fig. 5.2) as a function of temperature in the vicinity of critical temperature.

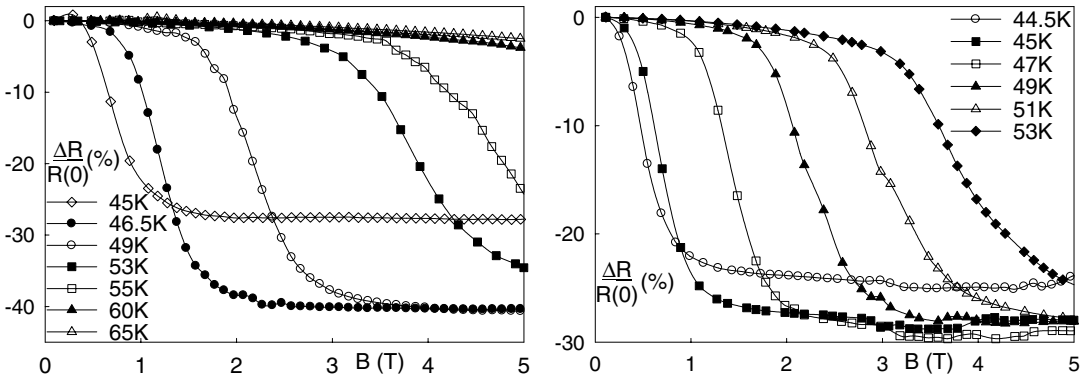

Figure A.7. Magnetoresistance of $ErCo_{1.94}Al_{0.06}$ and $ErCo_{1.94}Si_{0.06}$ at several selected temperatures above T_c.

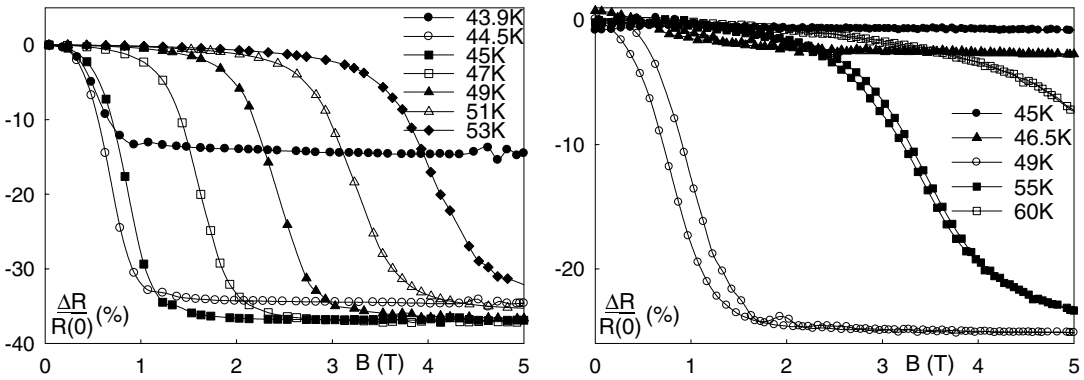

Figure A.8. Magnetoresistance of $ErCo_{1.94}Ga_{0.06}$ and $ErCo_{1.94}Ge_{0.06}$ at several selected temperatures above T_c.

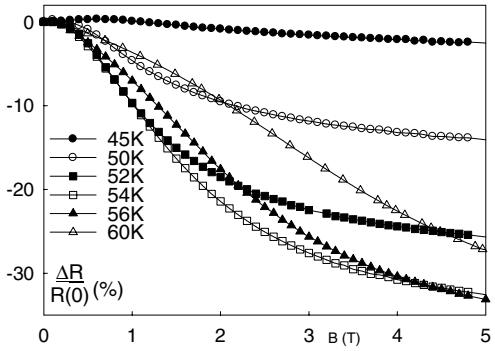

Figure A.9. Magnetoresistance of In–substituted sample at temperatures around T_c.

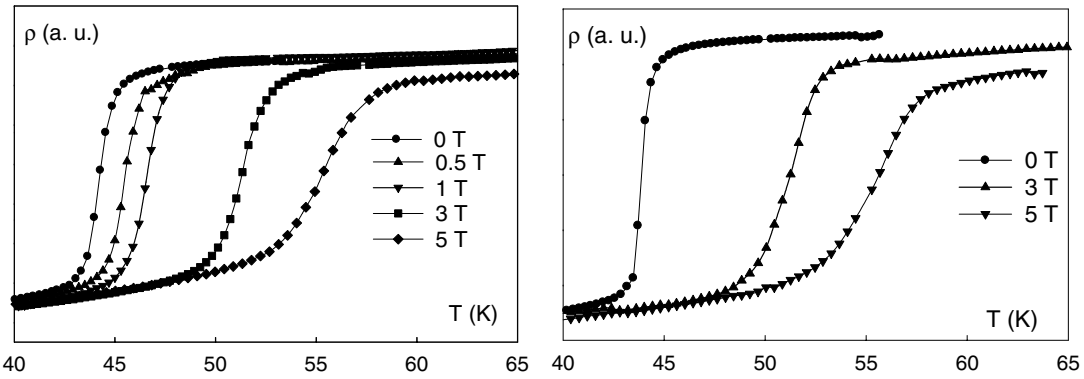

Figure A.10. Resistivity of $ErCo_{1.94}Al_{0.06}$ and $ErCo_{1.94}Si_{0.06}$ in field at temperatures around T_c.

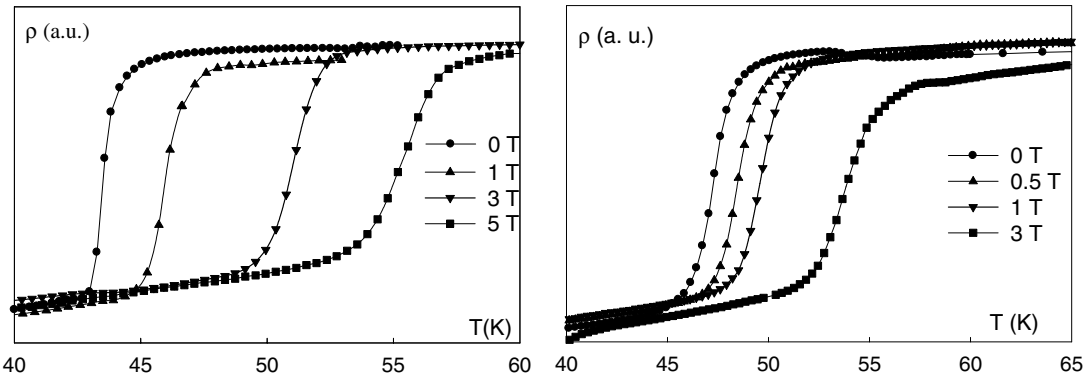

Figure A.11. Resistivity of $ErCo_{1.94}Ga_{0.06}$ and $ErCo_{1.94}Ge_{0.06}$ in field at temperatures around T_c.

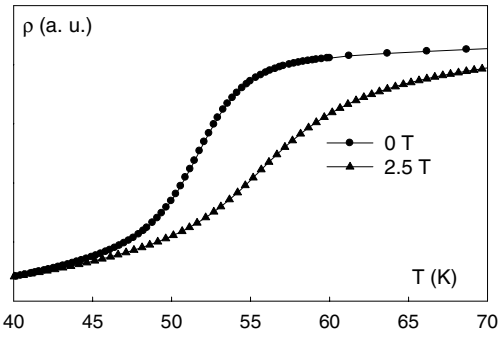

Figure A.12. Resistivity of In–substituted sample in field at temperatures around T_c.

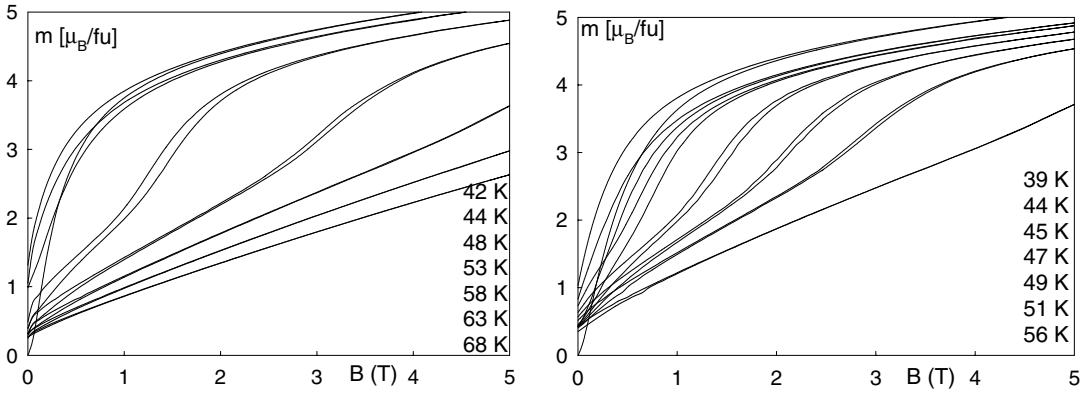

Figure A.13. Magnetization isotherms for $ErCo_{1.94}Al_{0.06}$ and $ErCo_{1.94}Si_{0.06}$.

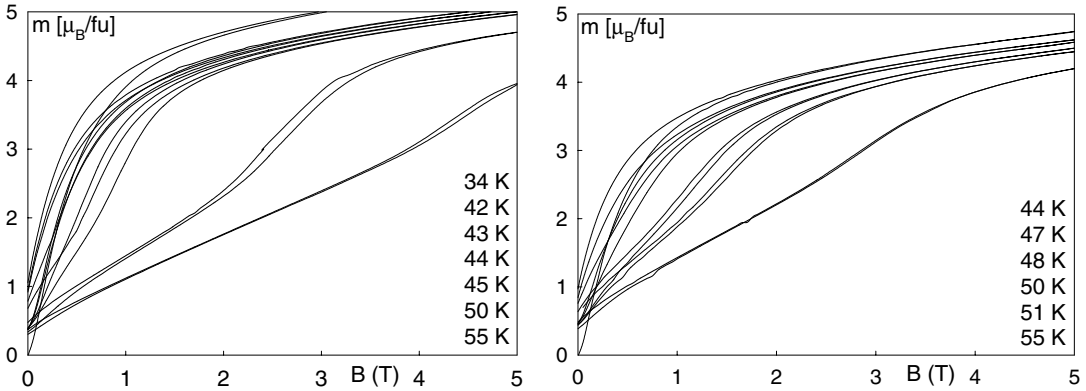

Figure A.14. Magnetization isotherms for $ErCo_{1.94}Ga_{0.06}$ and $ErCo_{1.94}Ge_{0.06}$.

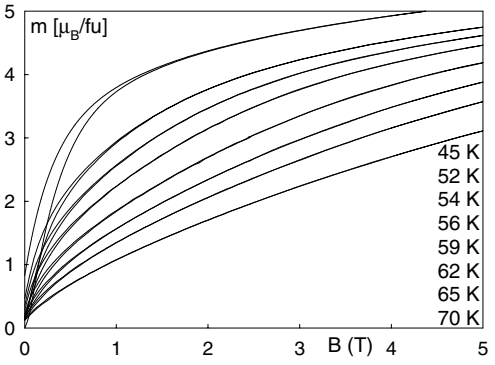

Figure A.15. Magnetization isotherms for $ErCo_{1.94}Ga_{0.06}$ and $ErCo_{1.94}In_{0.06}$.

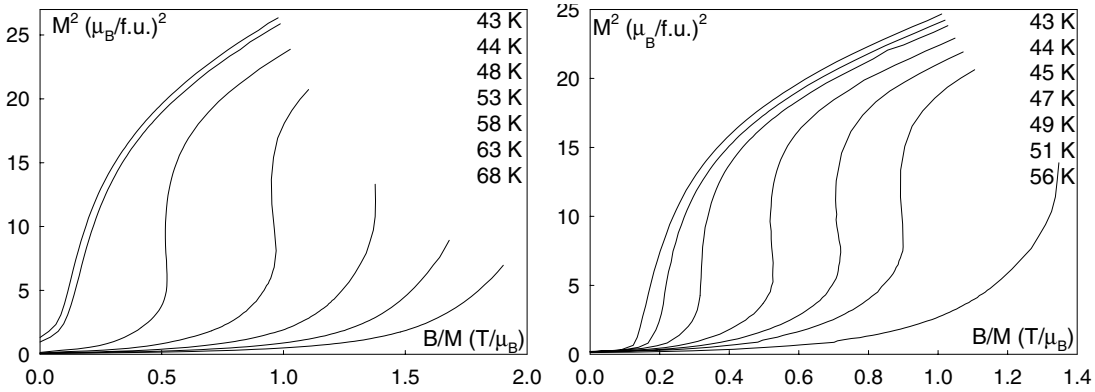

Figure A.16. Arrott plots corresponding to fig. A.13 for $ErCo_{1.94}Al_{0.06}$ and $ErCo_{1.94}Si_{0.06}$.

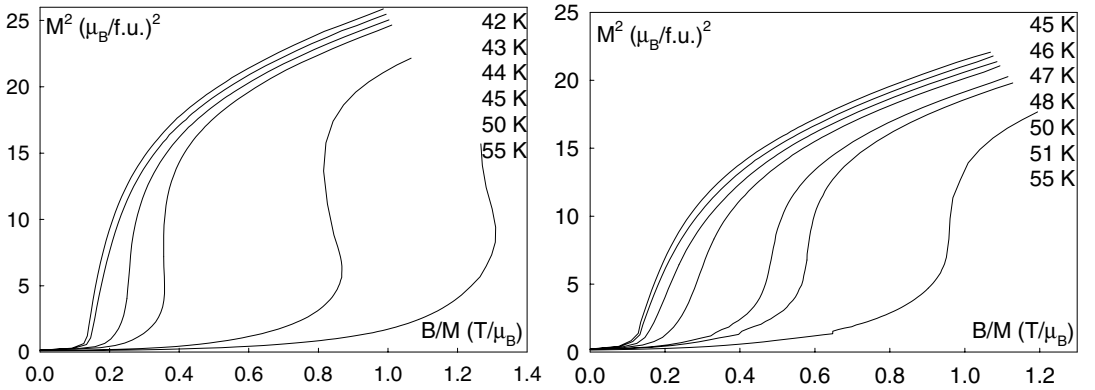

Figure A.17. Arrott plots corresponding to fig. A.14 for $ErCo_{1.94}Ga_{0.06}$ and $ErCo_{1.94}Ge_{0.06}$.

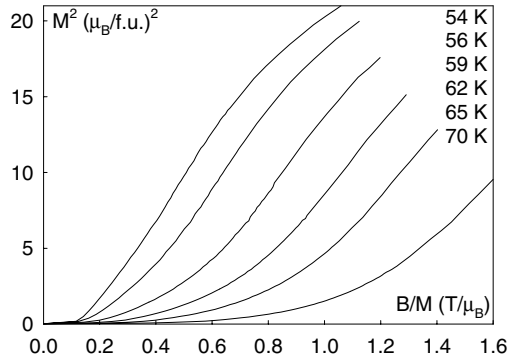

Figure A.18. Arrott plots corresponding to fig. A.15 for $ErCo_{1.94}In_{0.06}$.

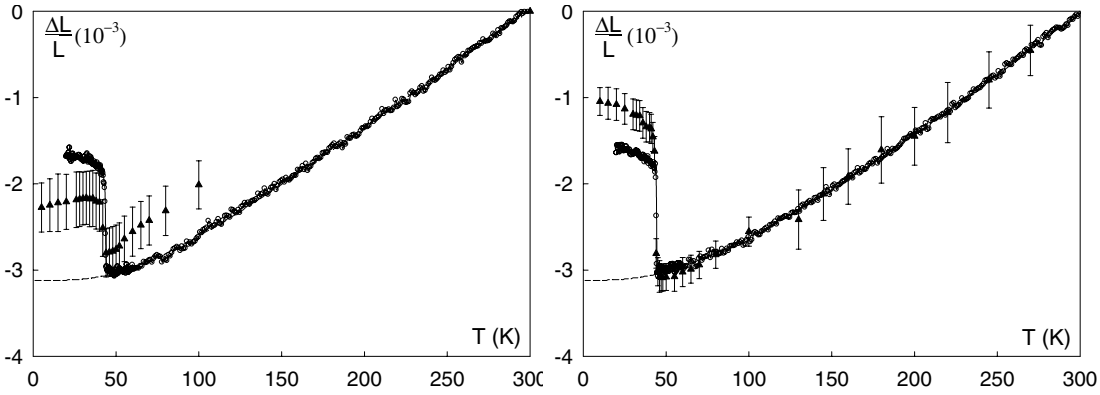

Figure A.19. Temperature dependence of the thermal expansion of $ErCo_{1.94}Al_{0.06}$ and $ErCo_{1.94}Si_{0.06}$.

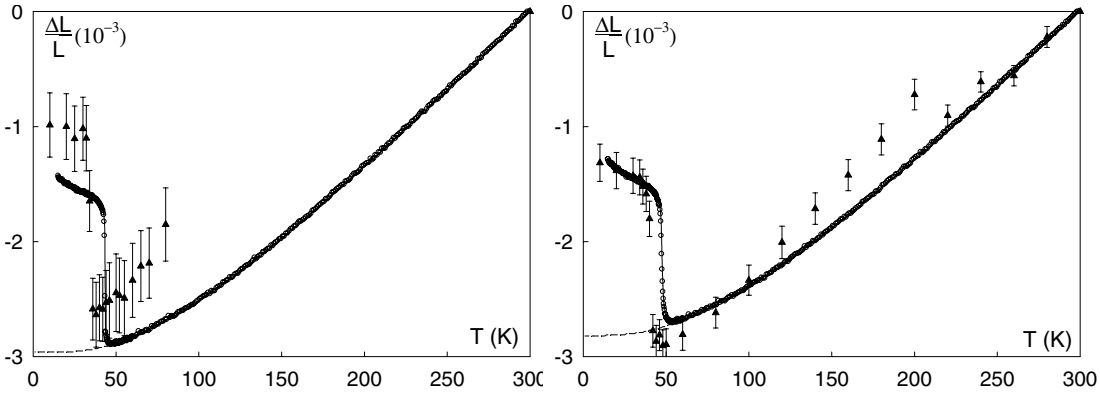

Figure A.20. Temperature dependence of the thermal expansion of $ErCo_{1.94}Ga_{0.06}$ and $ErCo_{1.94}Ge_{0.06}$.

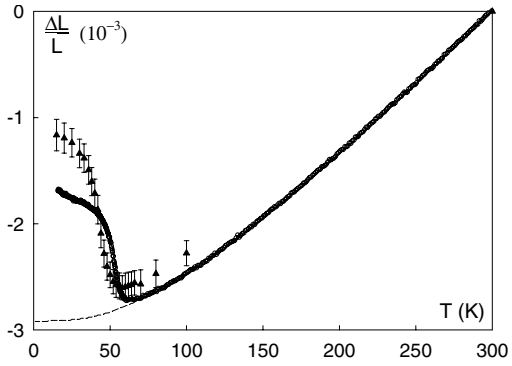

Figure A.21. Temperature dependence of the thermal expansion of $ErCo_{1.94}In_{0.06}$.

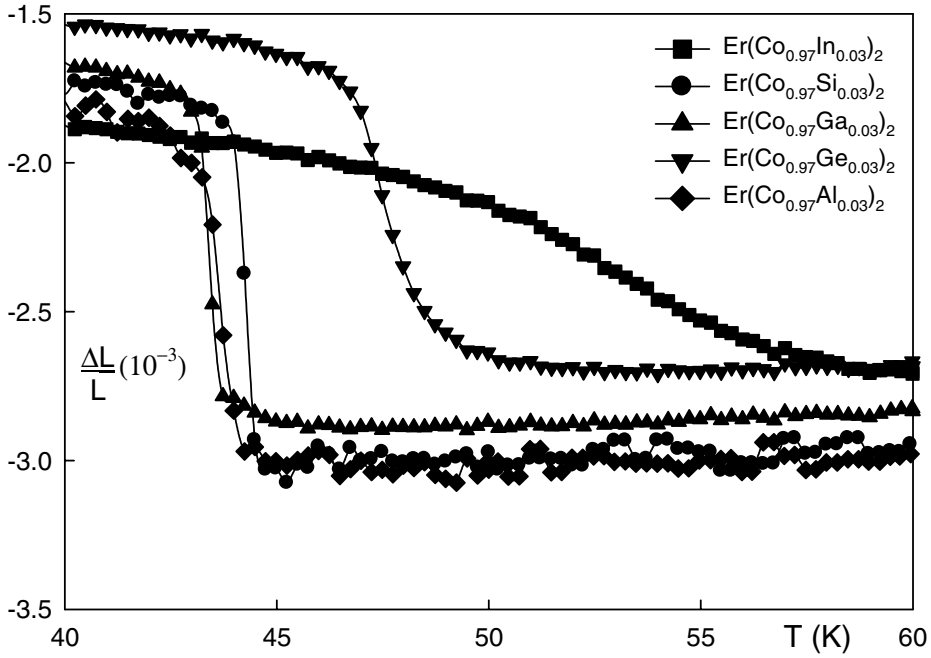

Figure A.22. Temperature dependence of the thermal expansion in the vicinity of the critical temperature.

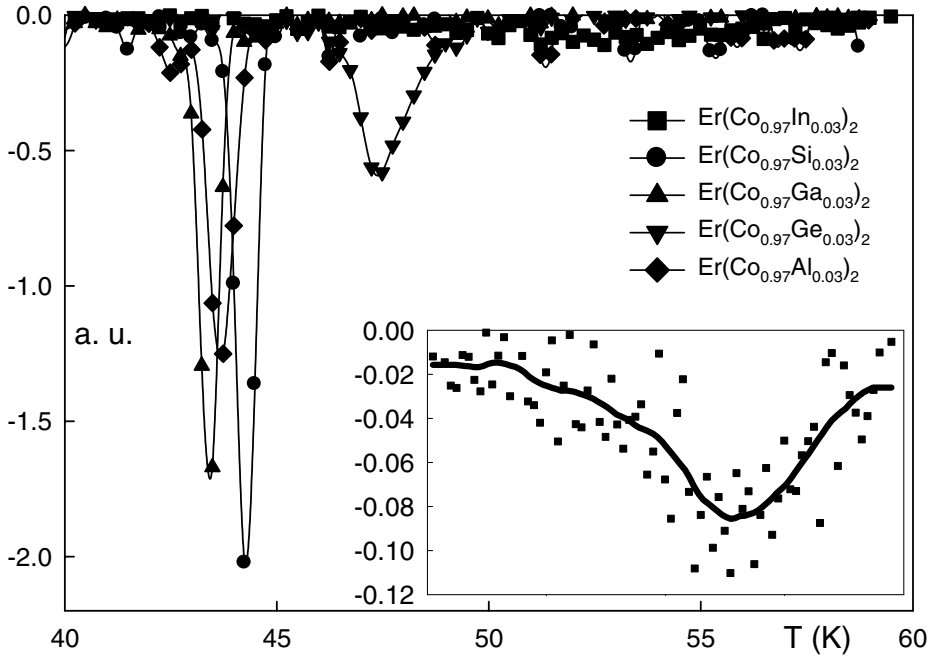

Figure A.23. Derivation of thermal expansion (fig. A.22) as a function of temperature in the vicinity of the critical temperature. Inset of figure is a plot for In substituted sample in the same temperature range, the line represents the smoothed data.

Bibliography

[1] Andersen N. H. (1979) *Phys. Rev. B* **19** 384

[2] Andreev A. V. (1995) *Thermal expansion anomalies and spontaneous magnetostriction in rare–earth intermetalics with cobalt and iron in Handbook of magnetic materials* ***8*** Elsevier Science Publishing

[3] Arrott A. (1957) *Phys. Rev.* **108** 1394

[4] Arrott A., Noakes A. E. (1967) *Phys. Rev. Lett.* **19** 786

[5] Baranov N., Gratz E., Nowotny H., Steiner W. (1983) *J. Magn. Magn. Matter.* **37** 206

[6] Barbara B., Gignoux D., Vettier C. (1988) *Lectures on moder magnetism* Springer Verlag Berlin

[7] Barron T. H. K., Collins J. G., White G. K. (1980) *Adv. Phys.* **29** 609

[8] Bloch F. (1929) *Z. Phys.* **57** 545

[9] Bloch D., Lemaire R. (1970) *Phys. Rev. B* **7** 2648

[10] Brooks M. S. S., Johansson B. (1993) *Density functional theory of the ground–state magnetic properties of rare earth and actinoids in Handbook of magnetic materials* ***7*** Elsevier Science Publishing

[11] Brož J., Roskovec V., Valouch M. (1980) *Fyzikální a matematické tabulky* SNTL Praha

[12] Cuong T. D. (1998) *Doctoral thesis* Charles University Prague

[13] Daniš S. (2002) *Doctoral thesis* Charles University Prague

[14] Dulal C. G., Raka B. (2002) *Int. J. Mol. Sci.* **3** 87

[15] Enser J. (2000) *Diplomarbeit* Technische Universität Wien

[16] Fukamichi K., Yokoyama T., Saito H., Goto T., Yamada H. (2001) *Phys. Rev. B* **64** 4401

[17] Goldschmidt V. M. (1926) *Naturwissenschaften* **14** 477

[18] Gunnarsson O. (1976) *J. Phys. F: Metal. Phys.* **6** 587

[19] Gratz E., Lindbaum A., Markosyan A.S., Mueller H. and Sokolov A. Yu. (1994) *J. Phys.: Condens. Matter* **6** 6699

[20] Gratz E., Resel R., Burkov A. T., Bauer E., Markosyan A.S. and Galatanu A. (1995) *J. Phys.: Condens. Matter* **7** 6687

[21] Gratz E., Markosyan A.S. (2001) *J. Phys.: Condens. Matter* **13** R385

[22] Gratz E., Markosyan A. S., Gaidukova I. Yu., Rodimin V. E., Berger St., Bauer E., Michor H. (2001) *Solid State Communications* **120** 191

[23] Goto T., Fukamichi K., Sakakibara T., Komatsu H. (1989) *Solid State Communications* **72** 945

[24] Goto T., Sakakibara T., Murata K., Komatsu K. and Fukamichi K. (1990) *J. Magn. Magn. Matter.* **90 & 91** 700

[25] Goto T., Katori H. A., Sakakibara T., Mitamura H., Fukamichi K. and Murata K. (1994) *J. Appl. Phys.* **76** 6682

[26] Hückel E. (1931) *Z. Phys.* **70** 204

[27] Janak J. F. (1977) *Phys. Rev. B* **16** 255

[28] Jullien R., Béal–Monod M. T., Coqblin B. (1974) *J. Phys. F: Metal. Phys.* **9** 1441

[29] Kasuya T. (1956) *Prog. Theory Physics* **16** 45

[30] Khmelevskyi S., Mohn P. (2000) *J. Phys.: Condens. Matter* **12** 9453

[31] Kittel C. (1985) *Úvod do fyziky pevných látek* Academia, Praha

[32] Klemm W., Bommer H. (1937) *Z. Anorg. Allg. Chem.* **231** 138

[33] Kohn W. and Rostocker N. (1954) *Phys. Rev.* **94** 1111

[34] Korringa J. (1947) *Physica* **14** 392

[35] Kroeger F. R., Swenson C. A. (1977) *J. Appl. Phys.* **48** 853

[36] Langevin P. (1905) *J. de Physique* **4** 678

[37] Mott N. F. (1935) *Proc. Phys. Soc.* **47** 571

[38] Moon R. M., Koehler W. C. (1965) *J. Appl. Phys.* **36** 978

[39] Morrish A. H. (1965; 2001) *The physical principles of magnetism* John Wiley & Sons; An IEEE Press Classic Reissue

[40] Murata K., Fukamichi K., Sakakibara T., Goto T., Katori H. A. (1992) *J. Phys.: Condens. Matter* **5** 2583

[41] Nowotny H., Gratz (2001) *Boltzmann equation and scattering mechanism in Encyclopedia of Materials: Science and technology* Elsevier Science Publishing

[42] de Oliveira N. A., Ranke P. J., Tova Costa M. V., Troper A. (2002) *J. Appl. Phys.* **91** 8879

[43] Pauli W. (1927) *Z. Phys.* **41** 81

[44] Rousseau J. J. (1998) *Basic crystallography* Wiley New York

[45] Ruderman M.A., Kittel C. (1954) *Phys. Rev.* **96** 99

[46] Seixas T. M., Machado da Silva J. M. (1999) *Physica B* **269** 362

[47] Shimizu M. (1982) *J. Phys. (Paris)* **45** 155

[48] Slater J. C. (1936) *Phys. Rev.* **49** 537

[49] Slater J. C. (1936) *Phys. Rev.* **49** 931

[50] Stoner E. C. (1936) *Proc. Roy. Soc. A* **154** 656

[51] Stoner E. C. (1938) *Proc. Roy. Soc. A* **165** 372

[52] Syshchenko O., Fujita T., Sechovský V., Diviš M., Fujii H. (2001) *J. Magn. Magn. Matter.* **226** 1062

[53] Svoboda P., private communication and spreeadsheet (based on polynomial interpolation of tabular data)

[54] Weiss P. (1907) *J. de Physique* **6** 667

[55] Wohlfarth E. P., Rhodes P. (1962) *Phil. Mag.* **7** 1817

[56] Yamada H., Shimizu M. (1989) *Physica B* **161** 179

[57] Yamada H. (1993) *Phys. Rev. B* **47** 11 211

[58] Yosida K. (1957) *Phys. Rev.* **106** 893

[59] http://www.vishay.com/brands/measurements_group/guide/tn/tn513/513index.htm

[60] http://www.webelements.com/

[61] ftp://charybde.saclay.cea.fr/pub/divers/fullprof.2k/

[62] ftp://charybde.saclay.cea.fr/pub/divers/winplotr/

[63] http://www.xray.cz/priv/kuzel/difpatan/

[64] http://www.qdusa.com/products/mpms.html

[65] http://www.qdusa.com/products/ppms.html

[66] http://www.qdusa.com/resources/pdf/ppmsappnotes/AR04.pdf